Retrograde Melting in Transition Metal-Silicon Systems: Thermodynamic Modeling, Experimental Verification, and Potential Application

by

David P. Fenning

B.S., Mechanical Engineering
Stanford University (2008)

Submitted to the Department of Mechanical Engineering
in partial fulfillment of the requirements for the degree of

Master of Science in Mechanical Engineering

at the

MASSACHUSETTS INSTITUTE OF TECHNOLOGY

September 2010

Author .....
Department of Mechanical Engineering
August 7, 2010

Certified by .....
Tonio Buonassisi
Assistant Professor of Mechanical Engineering
Thesis Supervisor

Accepted by .....
David Hardt, Professor of Mechanical Engineering
Chairman, Department Committee on Graduate Theses

Retrograde Melting in Transition Metal-Silicon Systems: Thermodynamic Modeling, Experimental Verification, and Potential Application

by

David P. Fenning

Submitted to the Department of Mechanical Engineering
on August 7, 2010, in partial fulfillment of the
requirements for the degree of
Master of Science in Mechanical Engineering

Abstract

A theoretical framework is presented in this work for retrograde melting in silicon driven by the retrograde solubility of low-concentration metallic solutes at temperatures above the binary eutectic. High enthalpy of formation of point defects in silicon leads to retrograde solubility for a number of solutes, including many 3d transition metals. The Ni-Si system is used to demonstrate that in silicon under supersaturated conditions, such solutes precipitate out into liquid droplets. Synchrotron-based X-ray Absorption Microspectroscopy measurements provide experimental confirmation of such phase transitions and the underlying thermodynamics. Finally, the potential for using retrograde melting to improve the electronic minority carrier lifetime of low quality silicon solar cell materials is considered.

Thesis Supervisor: Tonio Buonassisi
Title: Assistant Professor of Mechanical Engineering

Acknowledgements

I would like to thank my advisor Professor Tonio Buonassisi for his support and guidance over the past two years. I have learned a tremendous amount about photovoltaics, about asking good research questions, and about becoming a better scientist.

Also critical to the advancement of this research project were the lab postdocs, Bonna Newman and Mariana Bertoni. Not only would the synchrotron runs have been impossible without their help and thoughts during crunch time, but their guidance and insights during my progression in research has been invaluable. A big thank you is in order as well for our lab research scientists, Alexandria Fecych and Keith Richtman, for their helping hands and minds in and out of the lab.

I would also like to thank Matthew Marcus and Sirine Fakra for their expertise and extraordinary support in my data collection at beamline 10.3.2 at the Advanced Light Source.

And, of course I would like to thank my fellow students in the PV Lab, not just for their great ideas and their assistance in the lab and in the cleanroom, but also for their friendship. Work does not seem so much like work when you have such wonderful people around.

At the root of it all is the loving support from my family that helps so much when challenges present themselves, and in particular, I would like to thank you, Molly, for the many ways in which you support me and my work.

Contents

List of Figures

List of Tables

Chapter 1

Introduction

The potential for silicon photovoltaics to meet current and future energy demand is real. The solar resource, or the amount of power hitting the Earth's surface from the sun, is over 4,500x the power humans currently require [1]. Our current energy consumption from coal, natural gas, oil, nuclear, etc. all combined is like the amount of water in an average bathtub when the available solar energy is equivalent to an Olympic size swimming pool. The goal of the photovoltaics industry is to collect just a fraction of that incoming solar radiation and convert it directly into electricity for immediate use, for local storage, or for supplying power to the electrical grid.

Within photovoltaic technologies, devices based on crystalline silicon continue to dominate the market with a market share of about 78% as of 2008 [2]. In some ways, this investment and development of silicon photovoltaics is a byproduct of knowledge of the silicon system stemming from the success of the semiconductor industry, where silicon has been studied and engineered for over forty years to produce computer chips laden with ever-increasing densities of transistors [3]. On the other hand, silicon is a natural choice for photovoltaic devices. Silicon is the second most abundant element in the Earth's crust, meaning that there should be no shortage in supply of raw materials, and its semiconducting bandgap at ≈ 1.1 eV is nearly optimal for a single-junction photovoltaic device [4].

As the pressing concern of global climate change fuels interest from both consumers and producers in low-carbon energy technologies, the photovoltaic industry has grown

tremendously in recent years. Cumulative installed capacity increased from 0.386 GW in 1998 to 13,425 GW in 2008, while the annual rate of growth of installed capacity was 71% in 2008 [2]. The story of the industry remains a race to reduce the cost of photovoltaic power in a drive to reach grid parity, where the cost of solar power is less than or equal to the cost of power produced by the varied, often carbon-heavy sources supplying the grid [2].

While many pathways exist for reaching grid parity, a significant barrier for silicon solar cell manufacturers is the cost of the purified silicon feedstock which totals $\approx 15\%$ of the cost of producing a module [5]. One option toward reducing the cost of feedstock is to use poorer quality starting material, containing much higher levels of impurities [6–8]. Moving from high quality, semiconductor grade silicon to upgraded metallurgical silicon feedstock could reduce the cost of crystalline silicon modules by 11% using present technologies if device efficiency could be maintained despite the presence of higher levels of impurities [9].

The focus of my research is the study of such impurities – the physics that govern their interactions within the silicon crystal, their effect on the performance of devices, and the remediation of their impact through advances in processing techniques. In this work, I investigate the physics of, and discuss the potential applications for, a high-temperature phase transition of metal impurities in silicon known as *retrograde melting*, where the processing conditions force metal impurity atoms to cluster and precipitate out of solution into liquid metal-silicon droplets within the larger, solid silicon crystal.

1.1 Overview

In the following sections of Ch. 1, I will provide a short review of impurities in Si and their relevance to photovoltaic devices that motivates my research in retrograde melting in Si. I will also discuss previous research regarding retrograde melting in other materials systems and explain the experimental hypothesis of this work: that retrograde melting in silicon is directly observable as the precipitation of supersatu-

rated solid solutions of metal impurities in Si. In the following chapter, I will provide a thermodynamic model of retrograde solubility, which drives retrograde melting in Si. Next, I will explain the processing and preparation of the experimental samples, which will require an excursion into the details of our laboratory furnace setup. Then I will describe my further development of the laboratory's *in-situ* hot-stage, which I use to take synchrotron-based measurements of the absorption of Ni atoms in my Si samples in order to determine their chemical state and hence their phase. Finally, I will present the analysis and results of my experimental investigation of retrograde melting in the Ni-Si system using synchrotron techniques and will provide a discussion of the potential applications of retrograde melting to Si refining and solar cell processing.

1.2 Impurities in Silicon

Impurities in crystalline silicon can have a highly detrimental impact on semiconducting devices, even at concentrations as low as parts per billion [3, 10]. For example, the impact of iron on device efficiency is highlighted in Fig. 1-1 using data from the well-known late 1970s Westinghouse study of metal contamination in Czochralski-grown monocrystalline silicon solar cells by Davis *et al.*. While improved device processing and technological understanding has relaxed some of the strict requirements on silicon purity for solar cells, the 3d transition metals remain particularly pernicious in their effects because they create mid-gap defect energy levels that act as highly efficient recombination centers [11]. Many pathways also exist in the industrial environment for their incorporation into the crystal melt and ultimately solar cells, and their high solid-state diffusivities make it difficult to prevent their introduction during the high-temperatures inherent in solar cell manufacturing [12].

1.2.1 Recombination due to Impurities

The principal effect of metal impurities in semiconductors is to enhance the recombination of electron-hole pairs by creating deep level, midgap energy states [13, 14],

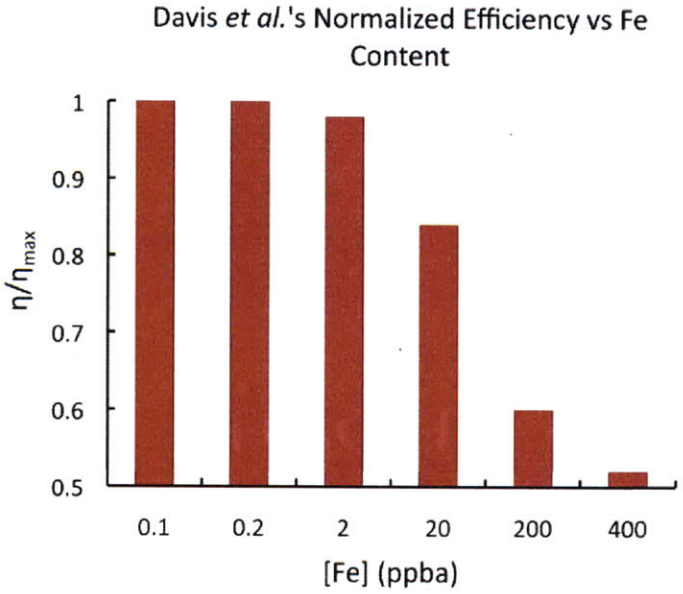

Figure 1-1: The strong negative impact of iron impurity concentration on device performance can be seen in the normalized efficiency data from Davis *et al.* [10]. Iron contamination at the level of 1 ppb is detectable in the performance data, and by 1 ppm, device efficiency is crippled by the presence of iron.

shown schematically in Fig. 1-2. This recombination mechanism is well described by the Shockley-Read-Hall model for recombination for many experimental conditions in silicon [15, 16]. According to the model, the recombination rate is governed by the energy level of the defect trap state with respect to the valence or conduction band, the density of defects in the material, and the capture cross-section of the defect. In the end, the effective minority carrier lifetime of the material, τ_{eff}, is the harmonic sum of the minority carrier lifetimes dictated by each type of recombination in the material: at point defects, at the surface of the sample, due to Auger recombination, etc.,

$$\frac{1}{\tau_{eff}} = \frac{1}{\tau_{Fe_i}} + \frac{1}{\tau_{surf}} + \frac{1}{\tau_{Auger}} .... \tag{1.1}$$

In multicrystalline ingots grown by directional solidification methods, impurity in-diffusion from the crucible lining of fast-diffusing metal impurities, *i.e.* Cu, Ni, Fe and Cr, causes a "red zone" of poor quality material around the edges, top, and

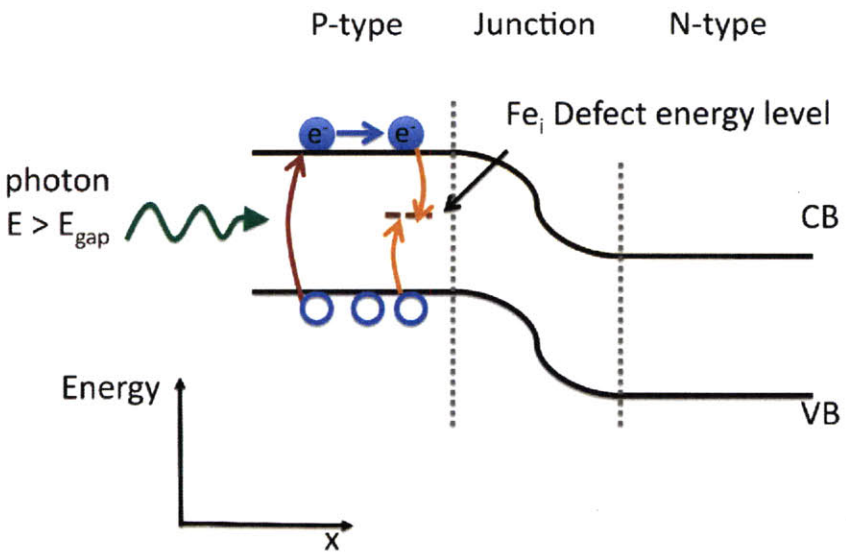

Figure 1-2: The defect energy level corresponding to an interstitial iron atom is show here in the middle of the bandgap. Such defect states in the bandgap create recombination centers that actively promote the recombination of excited carriers, reducing the conversion efficiency of the cell dramatically.

bottom of the ingot. Iron, in particular, because of its large capture cross section for electrons, degrades the material in the border region significantly [17]. This region of degraded materials actually affects a considerable fraction of all wafers produced by such methods [18].

Precipitated metals can also have an electronic impact [19]. However, in general because precipitates are sparsely distributed when compared to atomic point defects, dissolved impurities have a much larger impact on the material.

1.2.2 Spatial Distribution of Impurities in mc-Si

Not only the total concentration of impurities but also their distribution and density in the material is critical for establishing their electronic impact on the device [20, 21]. It has also been shown that the high-temperature processing involved in solar cell manufacturing can have large effects on the redistribution of metals and affects their

electronic impact on the device [22, 23].

Synchrotron-based x-ray microscopy previously has been used successfully to determine the elemental distributions of metal impurities and their chemical state within silicon solar cell materials [24–28]. In addition, coupling high-resolution spatial elemental maps obtained at the synchrotron with *in-situ* electrical measurements has allowed for the direct correlation of the presence of transition metal-silicide particles with low lifetime regions in the sample, particularly at structural defects such as grain boundaries [29, 30]. X-ray techniques and their application to retrograde melting will be discussed in detail in Ch. 5. For now, Fig. 1-3 from [22] suffices to illustrate

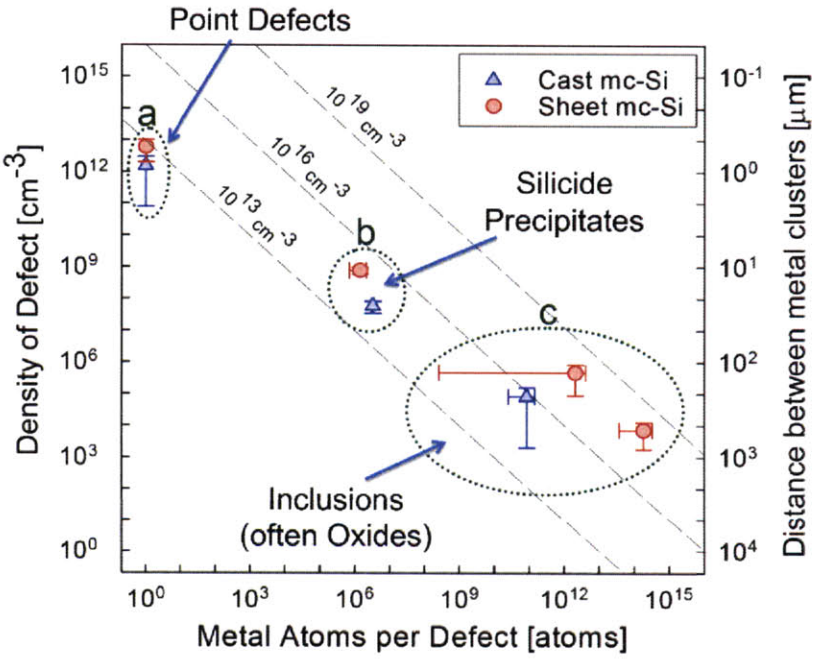

Figure 1-3: The density of impurity defects vs the number of atoms per defect is shown. Synchrotron-based microscopy techniques have allowed silicide and oxide precipitates to be directly observed using X-ray fluorescence microprobes. Point defects are unobservable because of the small number of atoms localized at the defect, but their high spatial density means that they strongly affect the electronic performance of the cell. Figure from [22].

the typical distribution of metals within silicon wafers. There are, in general, three classes of metal impurity defects in crystalline silicon: (1) atomic point defects where the metal atom is dissolved in solid silicon solution at low concentrations, (2) metal-

silicide second-phase precipitates that occur at much lower spatial density but are 10s of nanometers in size, and (3) inclusions from the manufacturing environment that enter the melt and often contain metal-oxides that are 100s or 1000s or nanometers in size. Point defects are the most problematic for electronic devices because their high spatial densities impede charge flow through the device. While precipitates do affect the minority carrier lifetime of the material as well, their impact is much less than point defects because of their lower densities (although their presence at pre-breakdown sites suggests silicide precipitates may cause detrimental shunting of the junction [31, 32]). Oxide inclusions have little electronic impact. In general, the lower the defect density, the better the performance of the solar cell.

1.2.3 Defect Engineering

In order to decrease the density of defects and improve the quality of solar cell materials, researchers in semiconductor and photovoltaic technology have developed a suite of process knowledge and annealing techniques collectively known as defect engineering. For metal impurities in silicon, defect engineering involves mainly metal impurity engineering, meaning the removal of impurities from the active device regions, or the reduction of defect densities. Both approaches reduce the deleterious effect of metals on the solar cell device performance. For a beautiful example of defect engineering, see Falster *et al.'s* publications [33, 34] regarding the controlled precipitation of SiO_2 particles in semiconductor industry wafers. Falster *et al.* created "magic denuded zones" by forming oxide precipitates away from the active device region and gettering metal impurities onto the oxide precipitates. With regard to photovoltaics, the silicon solar cell manufacturing process itself has also been tailored to allow for a number of steps aimed at gettering impurities.

Solid-to-liquid gettering

In multicrystalline silicon solar cell production, the first opportunity for gettering, and the largest absolute reduction in impurity levels, takes place during the growth

of multicrystalline ingots from the melt. The solidification furnace setup is designed so that heat escapes from the bottom of the crucible during solidification, such that the solidification front moves from the bottom of the crucible toward the top in a process known as directional solidification. The silicon recrystallization set-up and directional solidification is shown schematically in Fig. 1-4.

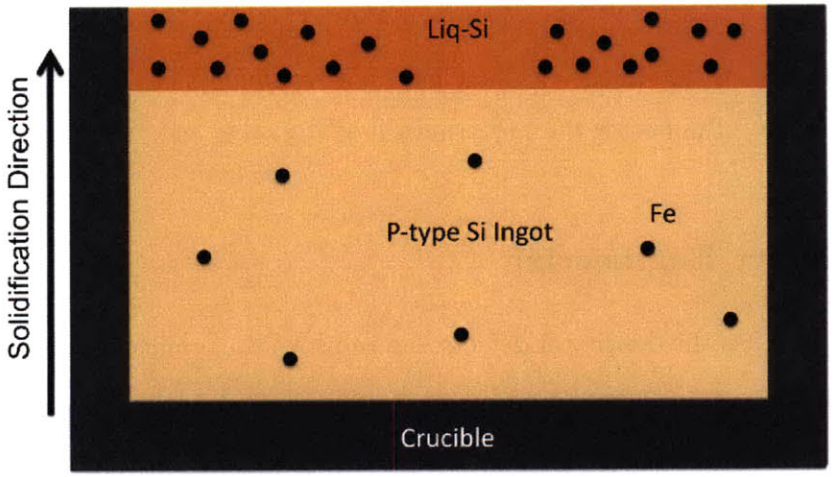

Figure 1-4: By cooling the molten silicon from the bottom of the crucible, the silicon crystal is grown from bottom to top, rejecting impurities from the resolidifying crystal into the melt due to thermodynamic segregation. The liquid Si becomes increasingly concentrated with impurities, and the distribution in the solidified ingot typically follows the Scheil equation.

The advantage of the directional solidification method comes from the thermodynamics of metal-silicon solutions, which causes a phenomenon known as solid-to-liquid gettering to occur. Liquid silicon can contain many orders of magnitude more of metal atoms in solution compared to the solid crystal [11, 18]. This ratio of thermodynamic solubilities is expressed as the segregation coefficient at the melting temperature, k_m:

$$k_m = \frac{S_{solid}}{S_{liquid}} \approx 10^{-4} - 10^{-6} \tag{1.2}$$

where S_{solid} and S_{liquid} are the solubility of metal impurity in solid silicon and in

liquid silicon at the melting temperature, respectively. For most metals in silicon, directional solidification thus results in a large reduction in the total metal concentration within the solid crystal throughout much of the ingot after solidification is completed, assuming no further introduction of metals into the system.

Assuming a well-mixed liquid, no solid state diffusion of metal impurities, and neglecting the back-diffusion of highly-concentrated liquid solutions of metal into the top of the solidified ingot, the distribution of metal impurity after directional solidification can be analyzed theoretically using simple mass conservation, producing the Scheil distribution:

$$C_s(x) = k_m C_o (1 - x)^{k_m - 1} \tag{1.3}$$

where C_s is the concentration of impurity at the ingot height, x, expressed as a fraction of the total ingot height, and C_o is the original concentration of impurity in the melt. The Scheil distribution resulting from the contamination of a silicon melt with 50 parts per million (ppm) of iron is shown in Fig. 1-5. The significant reduction in metal concentration in wafers coming from $< 80\%$ of the height of the ingot is the main feature of solid-to-liquid gettering. While multiple directional solidification steps would continue to reduce the concentration of impurities further, assuming high-purity growth conditions, the large energy inputs to heat and maintain the large silicon thermal mass at the melting temperature of silicon (1414 °C) makes multiple directional solidifications prohibitively expensive [35]. A typical temperature profile during crystal growth is shown in Fig. 1-6. One can plainly intuit the high cost of heating the growth furnace to such high temperatures for a daylong process. The tradeoff between purification and additional process costs is certainly a theme of silicon solar cell manufacturing.

Phosphorus diffusion gettering

Another instance of segregation gettering, known as phosphorus diffusion gettering, occurs during formation of the p-n junction during the manufacture of silicon solar cells. Phosphorus in-diffusion creates a space-charge region and an associated built-in

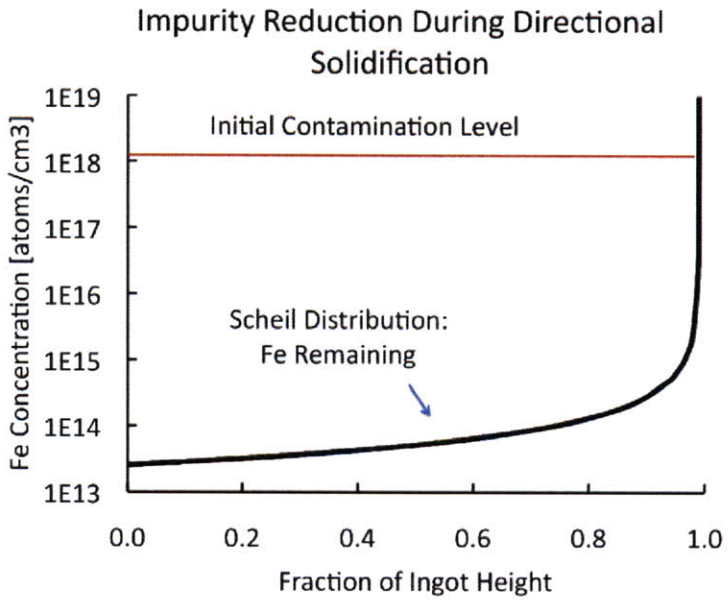

Figure 1-5: The dramatic reduction of metal concentration during solid-to-liquid segregation of metals as a result of directional solidification is exemplified by the behavior of iron. Shown here is the theoretical result of the contamination of an ingot with 50 ppm Fe, as indicated by the red line. The black line shows the resulting iron distribution in the ingot.

electric field that separates excited charges and allows the energy of carriers excited by solar radiation to be collected. Traditionally, p-n junction formation is carried out by the thermal diffusion of phosphorus into a boron-doped p-type wafer to form an $\approx 0.5 - 1\,\mu m$ thick n-type layer at the surface. Because of the high activation energy of diffusion for phosphorous, the diffusion is often carried out at temperatures above 800°C.

The high temperature involved in phosphorus diffusion allows another opportunity for the transformation of the metal distribution. In fact, the near surface highly-doped N-type layer acts as a sink for impurities because the solubility of many impurities is higher in the N-type layer than in the P-type bulk, yielding segregation gettering. A simple model of the phosphorus-dependent solubility of iron is developed in [37]. Phosphorus diffusion gettering can be highly effective at removing metal impurities from the bulk wafer in both monocrystalline and multicrystalline silicon [38–40].

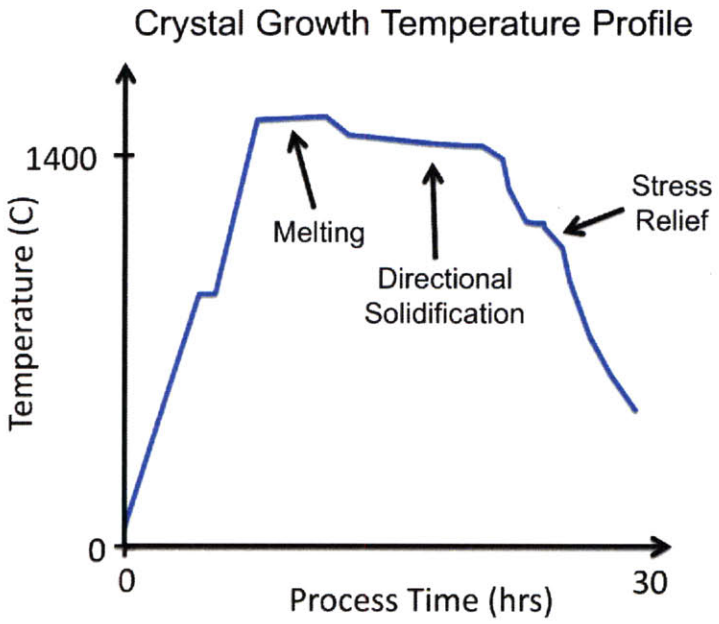

Figure 1-6: A typical growth temperature profile shown. More details on recently published thermal profiles during crystal growth in laboratory-scale furnaces are available in [18, 36].

Retrograde Melting

Retrograde melting, a phenomenon where a liquid second phase decomposes from a solid solution upon cooling, could offer another opportunity for solid-to-liquid segregation gettering. For many metallic interstitial solutes in silicon, the binary system exhibits a phenomenon known as retrograde solubility, where the maximum concentration of metal atoms in silicon solution occurs at a temperature higher than the eutectic temperature, the lowest temperature at which liquid can exist in the binary system. This is in contrast to many metallic systems, where the maximum solubility occurs at the eutectic temperature. Schematic examples of these two cases of solubility are shown in Fig. 1-7.

In metal-silicon systems, retrograde solubility can lead to supersaturated solutions when cooling a highly concentrated metal-in-silicon solution at temperatures above the eutectic point of the system because of the negative slope of the solvus line there. If the supersaturation leads to a chemical potential driving force greater than

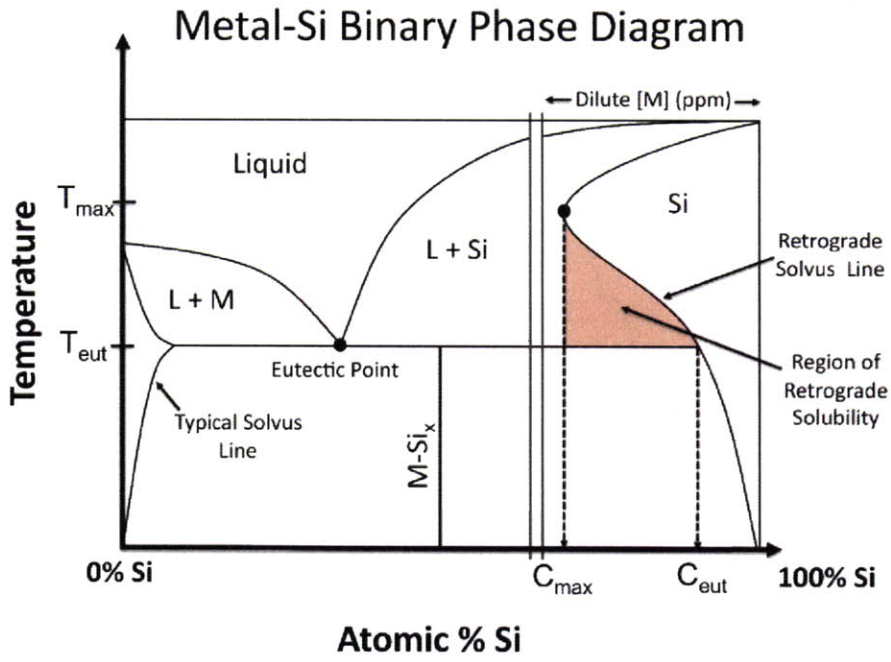

Figure 1-7: A schematic phase diagram for a metal-silicon system is shown. On the Si-rich side of the diagram, the scale of the diagram is changed to view the retrograde solvus line for the solid state solution of metal impurity in silicon. The dissolved metal concentration is often in the parts per million (ppm) range or less. The metal-rich side of the diagram shows a typical solubility curve with maximum concentration at the eutectic.

the nucleation energy barrier for precipitation, precipitation will occur. In the case of retrograde solubility, because the supersaturated system exists at temperatures above the eutectic temperature, precipitates will form in the liquid phase causing the phenomenon known as retrograde melting, where *local melting occurs upon cooling.*

Retrograde melting in silicon would thus create metal-silicon second-phase precipitates, nanometers in size and liquid in phase, distributed throughout the solid silicon matrix. There would remain a high concentration of metal in solution, since precipitation would proceed only as long as the solution remains supersaturated. However, as in Eq. 1.2, the solubility of metal solutes in liquid phase is generally orders of magnitude higher than in the solid state. Thus, solid-to-liquid gettering should drive many metal atoms still in solution into the liquid droplets, reducing the concentration of deleterious interstitial impurities in the bulk. Whereas the solid-to-liquid gettering

of metals during directional solidification occurs at the melting temperature as the solid-liquid interface passes through the melt, solid-to-liquid gettering caused by retrograde melting would occur during the cooldown from solidification as the solidified ingot becomes supersaturated with metal impurities down to the eutectic temperature of the metal-silicon system.

1.3 Previous Studies of Retrograde Melting in Other Systems

Retrograde melting has been observed in a variety of materials systems previously, including organic [41] and inorganic systems [42]. In many inorganic systems, the liquid phase arises out of the catatectic reaction at an invariant point in the phase diagram as discussed in Wagner and Rigney [43]. They consider a number of material systems that have phase diagrams containing a catatectic reaction whereby a solid phase, S_1 decomposes into a liquid phase, L, and different solid phase, S_2, according to:

$$S_1 \rightarrow L + S_2 \text{ during cooling} \tag{1.4}$$

Several such systems have been investigated more closely, such as Cu-Sn [44] and a number of rare earth metal-containing binary systems [45]. However, most common silicon-containing binary systems do not exhibit a catatectic reaction, and so retrograde melting in these systems would have to occur by another mechanism [46].

1.4 Proposed Retrograde Melting Pathway in Si

A similar pathway as has been observed for the ternary Sb-Bi-Te system has been proposed for the formation of liquid droplets by retrograde melting in silicon due to retrograde solubility of metal solutes in silicon above the eutectic temperature [47]. In the ternary system Sb-Bi-Te, of interest for its thermoelectric properties, retrograde melting has been observed to occur in the non-stoichiometric region near

the Sb_2Te_3 compound, as the solubility of Te in the solid compound decreases with temperature, leading to supersaturation of Te at temperatures above the system eutectic and subsequent formation of liquid [48]. The proposed retrograde melting pathway in Si is shown on the Si-rich side of the Ni-Si phase diagram in Fig. 1-8.

Following the hypothesis of [47], if one had a sample, denoted D in the figure, that was contaminated at the solubility corresponding to a temperature well above the eutectic temperature of the system, then upon cooling at a fixed concentration, the solution would supersaturate and precipitation would occur in the liquid phase to reduce the dissolved metal concentration to the limit allowed by the solvus line. Precipitation would increase as the temperature decreased until the solid metal-silicide forms. In the case of the Ni-Si system, $NiSi_2$ forms at 997 °C at the peritectic point shown on the diagram.

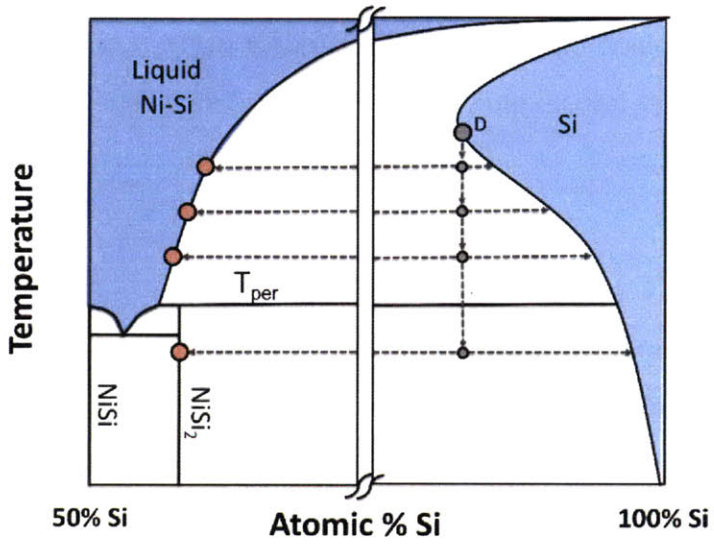

Figure 1-8: The proposed retrograde melting pathway for metal impurities that exhibit retrograde solubility in Si is shown on the Ni-Si phase diagram. Single-phase fields are shown in blue. A highly contaminated solid Si sample, designated as D, when cooled from high temperature contains more Ni atoms than the solid solution can hold. The excess Ni atoms are forced out of solution and precipitate as liquid droplets. Further precipitation occurs in the liquid phase as the sample cools. Finally, when the peritectic temperature is reached, the precipitates solidify into $NiSi_2$ particles.

To test this retrograde melting hypothesis, an *in-situ* high-temperature experiment was conducted by Hudelson *et al.* [49] examining the Cu-Ni-Fe-Si system along the Si edge to determine whether liquid precipitation upon cooling was experimentally observable using synchrotron-based absorption measurements. Retrograde melting was confirmed experimentally for the first time in Si by Hudelson *et al.* [49], although the complex quaternary nature of the system under investigation made the determination of the underlying mechanism difficult to establish conclusively.

1.5 Experimental Design

In this work, I conduct an experiment similar to that described in [49], but focus on the Ni-Si binary system to reduce the complexity of the analysis and with the aim of establishing a conclusive demonstration of the retrograde precipitation pathway. The Ni-Si system, shown in Fig. 1-9, is of particular interest because the solid silicide and high-temperature liquid phases are easily distinguishable via synchrotron-based absorption measurements, explained in further detail in Ch. 5. Moreover, Ni is a relatively benign metal impurity in dissolved form, as compared with Cu and Fe. Thus, the intentional introduction of Ni into feedstock materials in order to engineer the overall metal precipitate distribution via retrograde melting is not inconceivable.

During the proposed retrograde melting experiment along the Si edge of the Ni-Si system, several phase transitions are of note. The first is the proposed retrograde melting pathway that occurs when the supersaturation driving force due to cooling a saturated sample exceeds the nucleation energy barrier:

$$Si_{Ni}^{supersaturated} \rightarrow L_{Ni-Si} + Si_{Ni}^{eq} \tag{1.5}$$

Upon further cooling, the transition from a two-phase system containing liquid droplets (L + Si) to a totally solid system ($NiSi_2$ + Si) occurs via a peritectic reaction as seen in Fig. 1-9:

$$L_{Ni-Si} + Si \rightarrow NiSi_2 + Si \quad \text{Peritectic at 997°C} \tag{1.6}$$

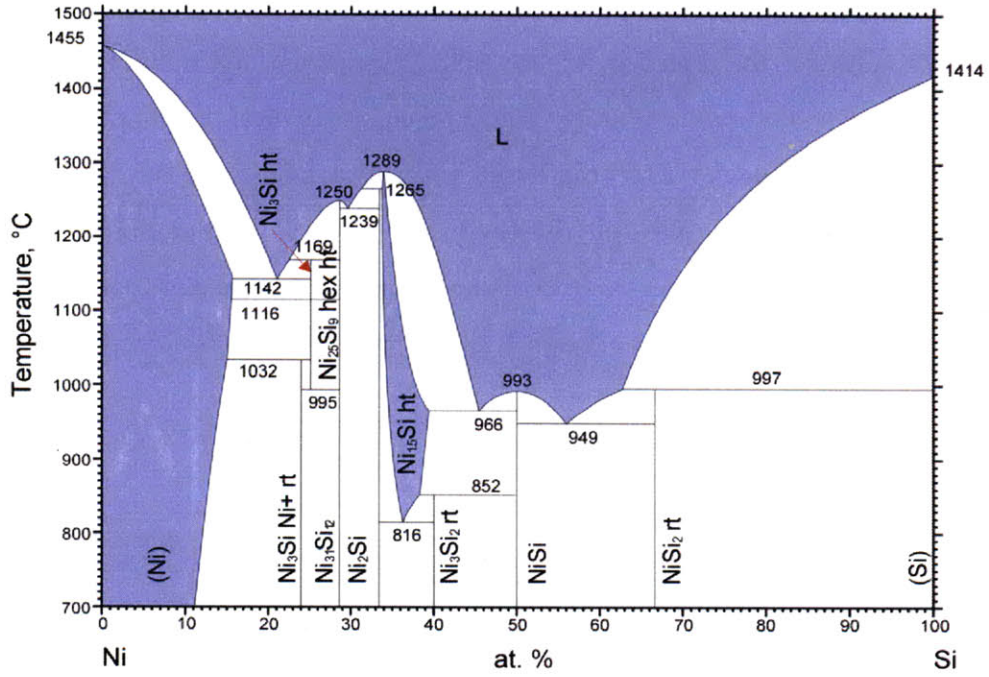

Figure 1-9: The high-temperature Ni-Si phase diagram. Theoretical calculations from [50, 51] , assembled in [52]. Note the peritectic and eutectic reactions that occur on the Si-rich side.

There also occurs a eutectic reaction on the Si-rich side of the phase diagram (see Fig. 1-9), in which the liquid phase at the eutectic point (949 °C) decomposes into two solid nickel-silicide phases according to:

$$L_{Ni-Si} \rightarrow NiSi + NiSi_2 \quad \text{Eutectic at 949°C} \tag{1.7}$$

Precipitation should occur according to Eq. 1.6 unless it is inhibited by a large nucleation energy barrier, discussed in further detail in Section 2.2.

1.5.1 Experimental Outline

To clarify the retrograde melting pathway, the experimental procedure is as follows:

- Contaminate Si samples with Ni at a range of temperatures above the eutectic temperature, as shown in Fig. 1-10;

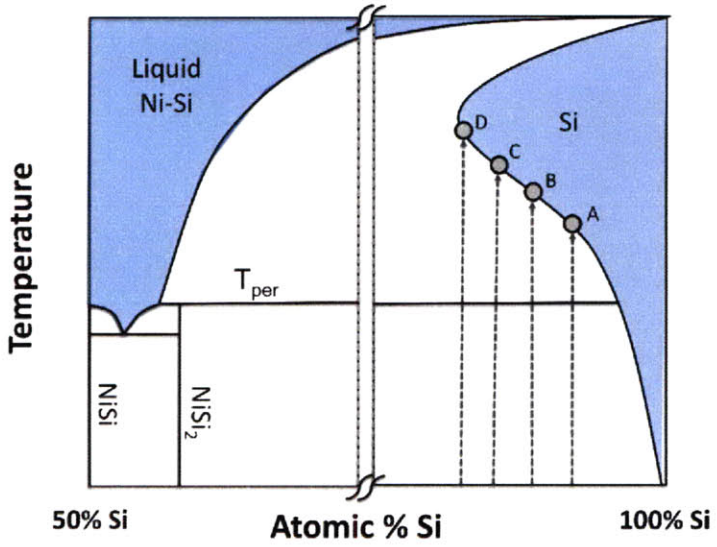

Figure 1-10: To test the proposed retrograde melting pathway, four Si samples are contaminated at different temperatures with Ni to produce samples along the solvus line for Si. The samples are then heated above the contamination temperature to ensure all the Ni atoms are dissolved in solid solution, and then the samples are cooled. Any precipitates that form are measured using synchrotron-based absorption techniques to determine whether they are solid or liquid.

- Heat the samples *in-situ* at the synchrotron to temperatures above the contamination temperature to fully dissolve the Ni;
- Cool the sample, allowing the solution to supersaturate, as shown in Fig. 1-8;
- As soon as precipitation is observed, measure the chemical state of the Ni-rich precipitates to determine whether they are liquid or solid;
- Continue to cool the sample, taking chemical state measurements until solidification of the precipitates is observed.

With an understanding of the proposed experiment and its importance to defect engineering in mind, I now turn to the thermodynamics of retrograde solubility to illuminate the underlying mechanisms driving the precipitation reactions in the Ni-Si system.

Chapter 2

Thermodynamic Modeling of Retrograde Melting

In this chapter, the classical macroscopic thermodynamics of solubility are examined first for metal-silicon systems on the Si-rich side at temperatures below the eutectic temperature. Then, the thermodynamic underpinnings of retrograde solubility are examined. Finally, an analysis of the driving force for retrograde melting is given.

2.1 Theory of Retrograde Solubility

2.1.1 Solubility below the Eutectic Temperature

Assuming a state of local equilibrium in the metal-silicon system, such that the thermodynamic state is well-defined, then the chemical potential of each component in each phase of the binary solution must be equal. In particular, the chemical potential of the metal in solution in solid silicon, designated here as the second component of the α phase, must be equal to the chemical potential of the metal atoms in the metal silicide phase, designated by β.

$$\mu_2^\alpha = \mu_2^\beta \tag{2.1}$$

The chemical potential of the ith component of the solution, μ_i, can in general be

written as:

$$\mu_i = \mu_i^o + kT\ln(\gamma_i X_i) \tag{2.2}$$

where μ_i^o represents the chemical potential of the ith component in a reference state and the second term of the equation is used to express the change in chemical potential due to the presence of i in solution, with atomic fraction X_i. The activity coefficient, γ_i, is used to account for deviation of the solution from ideality.

Rewriting Eq. 2.1 using Eq. 2.2 and grouping terms,

$$kT\ln(\gamma_2^\alpha X_2^\alpha) - kT\ln(\gamma_2^\beta X_2^\beta) = \mu_2^{\beta,0} - \mu_2^{\alpha,0} \tag{2.3}$$

The chemical potential is also identically equal to the partial free energy, which in turn can be written in terms of the partial enthalpy, h_i, and partial entropy, s_i

$$\mu_i = h_i - Ts_i \tag{2.4}$$

Breaking out the terms of the reference states, according to Eq. 2.4, we have:

$$kT\ln(\gamma_2^\alpha X_2^\alpha) - kT\ln(\gamma_2^\beta X_2^\beta) = (h_2^\beta - Ts_2^\beta)^o - (h_2^\alpha - Ts_2^\alpha)^o \tag{2.5}$$

Rearranging, we have:

$$kT\ln\left(\frac{X_2^\alpha}{X_2^\beta}\right) + kT\ln\left(\frac{\gamma_2^\alpha}{\gamma_2^\beta}\right) = -(h_2^\alpha - h_2^\beta)^o + T(s_2^\alpha - s_2^\beta)^o \tag{2.6}$$

Assuming an ideal solution with activity coefficient equal to unity, or a regular solution with ratio $\gamma_2^\alpha/\gamma_2^\beta \approx 1$, then:

$$\ln\left(\frac{X_2^\alpha}{X_2^\beta}\right) = \frac{T\Delta s_2^{\alpha,\beta} - \Delta h_2^{\alpha,\beta}}{kT} \tag{2.7}$$

where the fixed-concentration metal silicide state is used at the reference state, *viz.*

$$\Delta h_2^{\alpha,\beta} = h_2^{\alpha,o} - h_2^{\beta,o} \quad \text{and} \quad \Delta s_2^{\alpha,\beta} = s_2^{\alpha,o} - s_2^{\beta,o} \tag{2.8}$$

Here, $\Delta h_2^{\alpha,\beta}$ represents the energy required to transform an atom of 2 from the β phase to the α phase, or in other words, the enthalpy of formation of the metal point defect with reference to the silicide. Similarly, $\Delta s_2^{\alpha,\beta}$ is the entropy of formation of the point defect. Alternatively, we can write:

$$\ln\left(\frac{X_2^{\alpha}}{X_2^{\beta}}\right) = \frac{-\Delta g_2^{\alpha,\beta}}{kT} \tag{2.9}$$

Since the composition of the metal silicide phase, X_2^{β}, is constant with temperature as seen in Fig. 1-7, Eq. 2.9 yields the familiar Arrhenius relationship of metal solubility in silicon with temperature, with $\Delta g_2^{\beta,\alpha}$ equal to the activation energy for formation of the metal solute defect.

2.1.2 Solubility above the Eutectic Temperature

In contrast to metal silicide-silicon solvus line analyzed in Section 2.1.1, the solvus line at temperatures above the eutectic temperature separates the liquid metal-silicon + solid silicon two-phase field from the solid silicon phase as seen in Fig. 1-7. We can rewrite Eq. 2.7 accordingly, using superscripts l and s to denote the liquid and solid phases respectively, following the thermochemical derivation from [11] wherein the heat capacity difference between the solid and the liquid phases is neglected and the metal in silicon solution is considered ideal:

$$\ln\left(\frac{X_2^{s}}{X_2^{l}}\right) = \ln k = \frac{T\Delta s_2^{s,l} - \Delta h_2^{s,l}}{kT} \tag{2.10}$$

where k is the distribution coefficient. The solid solubility of the metal solute can then be calculated by:

$$X_2^{s} = kX_2^{l} = k(1 - X_1^{l}) \tag{2.11}$$

Assuming an ideal silicon solution, the liquidus line depends only on the enthalpy and entropy of fusion of silicon, ΔH_1^f and ΔS_1^f respectively,

$$X_1^l = \exp\left(-\frac{\Delta H_1^f - T\Delta S_1^f}{kT}\right) \tag{2.12}$$

Finally, plugging Eqs. 2.10 and 2.12 into the Eq. 2.11 to calculate the solid solubility of metal in silicon above the eutectic temperature, we have:

$$X_2^s = \exp\left(\frac{T\Delta s_2^{s,l} - \Delta h_2^{s,l}}{kT}\right)\left[1 - \exp\left(-\frac{\Delta H_1^f - T\Delta S_1^f}{kT}\right)\right] \tag{2.13}$$

2.1.3 Alternative Derivation of Retrograde Solubility

While Weber employs Eq. 2.13 to calculate the solubility of 3d metals in silicon [11], the excess partial enthalpy and entropy terms suffer for clarity. In order to increase our understanding of the retrograde solubility phenomenon, we can follow the analysis of [53]. Therein, it is assumed that the solid solution is a regular solution, such that the partial enthalpy, h_2^s, is a constant and the partial entropy, s_2^s is ideal. Then,

$$h_2^s = kT \ln \gamma_2^s \tag{2.14}$$

Along the solvus line, where the solid solution is in equilibrium with an assumed ideal liquid solution, rewriting Eq. 2.3, we have:

$$\mu_2^{s,o} + kT \ln X_2^s + h_2^s = \mu_2^{l,o} + kT \ln X_2^l \tag{2.15}$$

Using the pure solid of component 2 as the reference state, then,

$$\mu_2^{l,o} - \mu_2^{s,o} = h_2^f - Ts_2^f \tag{2.16}$$

where h_2^f and s_2^f are the enthalpy and entropy of fusion of the solid component 2. Again, this assumes that the solid and liquid thermal capacity are negligibly different

in the range of temperatures of interest. Rewriting Eq. 2.15 using Eq. 2.16, we obtain

$$\ln\left(\frac{X_2^s}{X_2^l}\right) = \left(\frac{h_2^f - h_2^s - Ts_2^f}{kT}\right) \tag{2.17}$$

Finally, writing the solid solubility of the metal impurity in silicon using Eqs. 2.11, 2.12, and 2.17, we obtain:

$$X_2^s = \exp\left(\frac{h_2^f - h_2^s - Ts_2^f}{kT}\right)\left[1 - \exp\left(-\frac{\Delta H_1^f - T\Delta S_1^f}{kT}\right)\right] \tag{2.18}$$

Written in this manner, we can see that any retrograde behavior is a result of the magnitude of the formation enthalpy of the metal impurity point defect, h_2^s, with respect to the magnitude of the enthalpy of fusion, h_2^f, as shown in [54]. The large energy required for dissolution increases the dissolved concentration above the eutectic temperature until very high temperatures are reached creating the region of retrograde solubility as shown in Fig. 1-7.

2.1.4 The Point of Maximum Solid Solubility

By differentiating Eq. 2.18 with respect to temperature, following the procedure outlined in [11], one can find the temperature of maximum solubility of metal impurity:

$$T_{max} = \frac{\Delta H_1^f/k}{\Delta S_1^f/k - \ln\left(\frac{h_2^f - h_2^s}{h_2^f - h_2^s - h_1^f}\right)} \tag{2.19}$$

2.2 The Driving Force due to Supersaturation

When the solution becomes supersaturated due to cooling at fixed concentrations, the solution can be maintained in a single-phase, metastable state by the presence of a nucleation energy barrier to precipitation.

The reduction in free energy per atom, *i.e.* the driving force for precipitation, f, that could be achieved by precipitation of a second phase and a return to the equilibrium solute concentration from the quasi-equilibrium, single phase state can

be described by the excess chemical potential associated with the supersaturated condition:

$$
\begin{aligned}
f &= \mu_2 - \mu_2^{eq} && (2.20)\\
&= [\mu_2^o + kT\ln(\gamma_2 X_2)] - [\mu_2^o + kT\ln(\gamma_2 X_2)]^{eq} && (2.21)\\
&= kT\ln\left(\frac{\gamma_2 X_2}{\gamma_2^{eq} X_2^{eq}}\right) && (2.22)
\end{aligned}
$$

Assuming that the activity coefficient for solute atoms remains approximately unchanged before and after precipitation, we write:

$$
\begin{aligned}
f &= kT\ln\left(\frac{X_2}{X_2^{eq}}\right) && (2.23)\\
&= kT\ln\left(\frac{Vc_2}{V^{eq}c_2^{eq}}\right) && (2.24)
\end{aligned}
$$

with V the average atomic volume and c_2 the concentration of the solute. Assuming a negligible change in average atomic volume, V, we have the driving force for precipitation in terms of the solute concentration, c_2:

$$
f = kT\ln\left(\frac{c_2}{c_2^{eq}}\right) \qquad (2.25)
$$

2.2.1 Nucleation Energy Barrier

According to the classical model of nucleation, the free energy of the system as a whole can be broken into bulk and interfacial terms. The creation of interface due to the formation of a second-phase particle increases the energy of the system. However, a decrease in free energy also occurs due to a reduction of the bulk chemical potential by precipitation of the second phase. If negative, the volumetric bulk term can overcome the positive, areal interfacial term, and the second-phase particle will remain stable.

In general, a critical nucleus size is required to achieve the necessary reduction in free energy, and the energy required to agglomerate this critical nucleus of atoms is known as the nucleation energy barrier as shown schematically in Fig. 2-1.

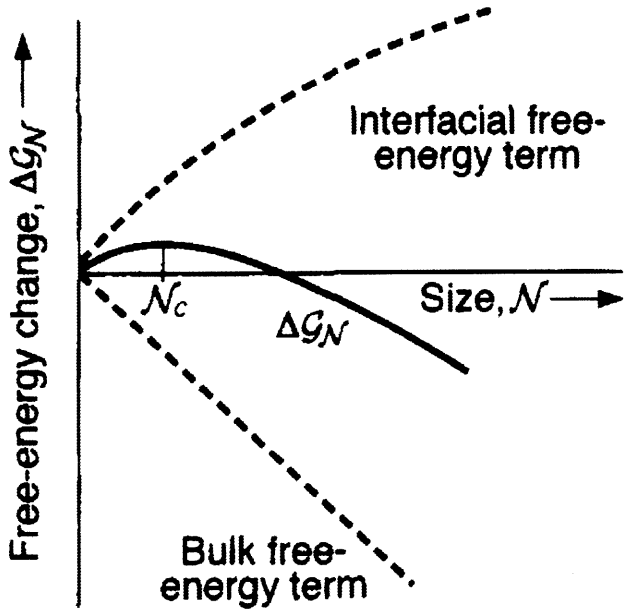

Figure 2-1: The reduction in free energy due to the change in chemical potential of the bulk must overcome the large surface area-to-volume ratio of the second-phase nucleus and the associated interfacial free-energy term in order to achieve stability. Figure from [55].

2.3 Assumptions and Discussion of Model

2.3.1 Ideal Solution

In the model presented above, the solution of metal impurity in silicon was considered ideal, although most solutes in Si exhibit some departure from ideality [56]. A more detailed calculation of the driving force for nucleation should be possible with a more thorough thermodynamic dataset and available computational tools [57], but the simplicity of Eqn. 2.25 lends itself to the easy adoption of the concepts of retrograde melting mechanism while deviations from ideality are typically small at such low solute concentrations.

2.3.2 Thermodynamic Equilibrium

The requirements for thermodynamic equilibrium are the maintenance of mechanical, thermal, and chemical equilibria. Within the experimental system, changes in mechanical pressure are very small, particularly with respect to the speed of sound in solid silicon. Thus, we can be assured that mechanical equilibrium is maintained. Considering thermal equilibrium, the system is certainly changing in temperature as the sample is heated and cooled within the hot stage. However, because of the high thermal conductivity of silicon and the low thermal mass of the Si samples, the relatively low heating and cooling rates of <5°C/min allows for the local equilibrium assumption to be applied to good effect because thermal gradients within the sample are small. Finally, the chemical reactions that take place during precipitation appear to occur from accumulated experience at rates much faster than the characteristic time of the experiment, such that an assumption of chemical equilibrium at all times is also appropriate.

2.3.3 Nucleation Energy Barriers

The nucleation energy barrier to precipitation can be effectively lowered by creating a high energy surface or interface, *i.e.* creating a favorable heterogeneous nucleation site. In this experiment, a large defect on the sample surface is created by scratching the surface with a diamond scribe. Given the variety of heterogeneous nucleation sites provided by the mechanical scratching of the sample surface, it would be expected that the nucleation energy barrier to precipitation of second phase silicides would be quite low [58].

Chapter 3

Sample Selection and Preparation

3.1 Sample selection

A float-zone (FZ), monocrystalline silicon wafer was chosen to produce the samples so we could reduce unintentional metal impurity defects and avoid structural defects like grain boundaries and dislocations that could affect the kinetic and/or thermodynamic environment of the experiment.

3.2 Sample preparation

The experimental Ni-contaminated samples were prepared for the *in-situ* synchrotron experiment following the procedure outlined in Fig. 3-1. Details of each process step are given below.

Laser Cutting

A large set of 5x5 mm experimental samples were scribed by a customized, 1064 nm Electrox laser cutter from a P-type (100) wafer with a resistivity of 10-200 $\Omega - cm$. The size of the cup in the heating element of the *in-situ* hot stage (to be described in detail below) dictated a 5x5 mm sample size. The samples were 675 μm thick and were single-side polished. The FZ wafer was placed on a clean piece of glass as a substrate during laser cutting. Because the wafer was so thick, the sample was scribed

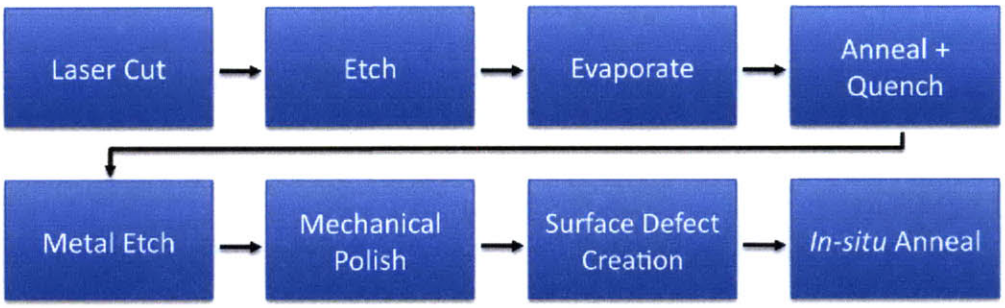

Figure 3-1: Sample preparation flow diagram for the retrograde melting experiment.

$\approx 300\mu m$ deep, after which they were cleaved manually using clean glass slides as the cleaving edges. The wafer was cleaved into 5 pieces, each 10x20 mm and containing 8, 5x5 mm samples, with one piece to be processed for use as the synchrotron chemical state measurement standard, designated the "Standard" sample, and the other four pieces, the experimental samples, designated Samples A, B, C, and D.

Surface Etch for Cleanliness

The samples were cleaned prior to evaporation of a metal surface layer by organic solvents, followed by a rinse in deionized (DI) water. Finally, the samples were dipped in a solution of 10% HF for 30 seconds to remove the native oxide layer.

Ni Deposition

Within 30 minutes after the HF dip, the samples were moved to the vacuum chamber of a Sharon E-beam evaporator in order to avoid the regrowth of a substantial native oxide [59]. A 1 μm layer of Ni was evaporated onto the unpolished side of the samples from a high-purity Ni target. The sample cleaning and evaporation was performed at the Harvard Center for Nanoscale Systems. The standard sample was set aside for synchrotron measurement.

Ni In-Diffusion

The experimental samples, A-D, were then in-diffused with Ni from the evaporated surface layer by annealing in a forming gas ambient in the high-temperature furnace. The in-diffusion of the samples was carried out using the furnace setup and the annealing procedure described in detail in Ch. 4. Prior to the anneal, the samples were broken in half, so that one half could be taken to the synchrotron and the other half could serve as an experimental control of the contamination anneal. These control samples were later sent for inductively-coupled plasma mass spectroscopy (ICP-MS) to measure the total concentration of metals within the samples. Details on the temperature corresponding to each anneal are listed in Table 3.1. Unfortunately, no thermocouple reading was taken for sample C.

Sample	Desired Temp (°C)	Set Temp (°C)	TC Reading (°C)
A	1025	1070	1012
B	1075	1120	1110
C	1125	1170	–
D	1225	1280	1229

Table 3.1: Experimental Samples and Their Annealing Temperatures

Two events worth noting took place during the annealing. For Sample D, during the quench, the silicone oil appeared to exceed its flash point and ignite when the sample hit the surface. Once the sample submerged, no further flames were observed, though bubbles rose to the surface, perhaps indicating a phase change occurring. Secondly, for Sample C, during the anneal the experimental half of Sample C fell onto the ICPMS control sample half. After quenching, the two halves were effectively fused together, indicating that a liquid Ni-Si layer definitely formed on the sample surface with evaporated metal. Sample C was the only sample for which the two halves fused together, which may have potentially changed the heat transfer during the quench.

Metal Etch

After quenching, the samples were removed from the oil and washed thoroughly with deionized water. They were then etched in a mixture of 10% HCL in water to remove any remaining metal surface layer. Sample C had a particularly stubborn silicide layer form on its surfaces. In an attempt to remove this layer, which could have contaminated the surface of the sample during polishing, the sample was stirred for 30 seconds in H_2O_2 to oxidize the surface aggressively, then was etched in H_2SO_4 to remove the silicide layer.

Mechanical Polishing

To improve signal-to-noise ratio during measurement, I wanted to eliminate the dispersion of precipitating atoms to heterogeneous nucleation sites scattered across the surface of the sample. Therefore, to avoid *uncontrolled* out-diffusion of the Ni impurity population during reheating *in-situ*, the samples were carefully polished to eliminate potential heterogeneous nucleation sites. The samples were double-sided polished using SiC grinding papers to a roughness of 5 μm on a Bueller polisher, after which the samples were polished manually using diamond pastes down to 1/4 μm roughness, whereupon they were polished with a 50 nm alumina suspension.

Creating Surface Defects for Heterogenous Nucleation

Once finely polished, a preferred nucleation site for concentrating the precipitating Ni atoms upon supersaturation was created on the front of the sample by scribing the surface with the fine tip of a diamond scribe. The resulting scratch contained highly damaged material, offering a high density of potential nucleation sites. Diamond scribing was decided on as the preferred method for creating surface defects after a SEM and EDS analysis of a laser-scribed and reannealed sample revealed no observable Ni precipitates, suggesting that the laser scribe did not act as a preffered nucleation site - instead the unpolished edges of the sample probably out-competed the laser scribe for nucleating precipitates.

Chapter 4

Processing Furnace Setup and Annealing Procedure

4.1 Furnace Setup

The thermal annealing experimental procedure used was similar to that in Istratov *et al.*'s [60, 61] studies of precipitation of metal silicides in silicon. A Carbolite high-temperature furnace was used to anneal the sample in a vertical furnace orientation so that I could quench the samples from high temperature to room temperature within seconds by dropping the samples from the hot zone of the furnace into a beaker filled with silicone oil. The typical arrangement of furnace equipment for quenching experiments is shown schematically in cross-section in Fig. 4-1. Silicone oil is chosen as the quenching agent because it has been shown to provide a cooling rate of $\approx 200K/s$ without significant risk of shattering the sample due to large thermal gradient from too large a cooling rate [62].

A new sample holder of high-purity quartz was used. The entire quartz sample holder was dipped in 5% HF for 10 seconds, then rinsed in DI water, in order to etch off the surface layer which may have been contaminated by packaging in transit.

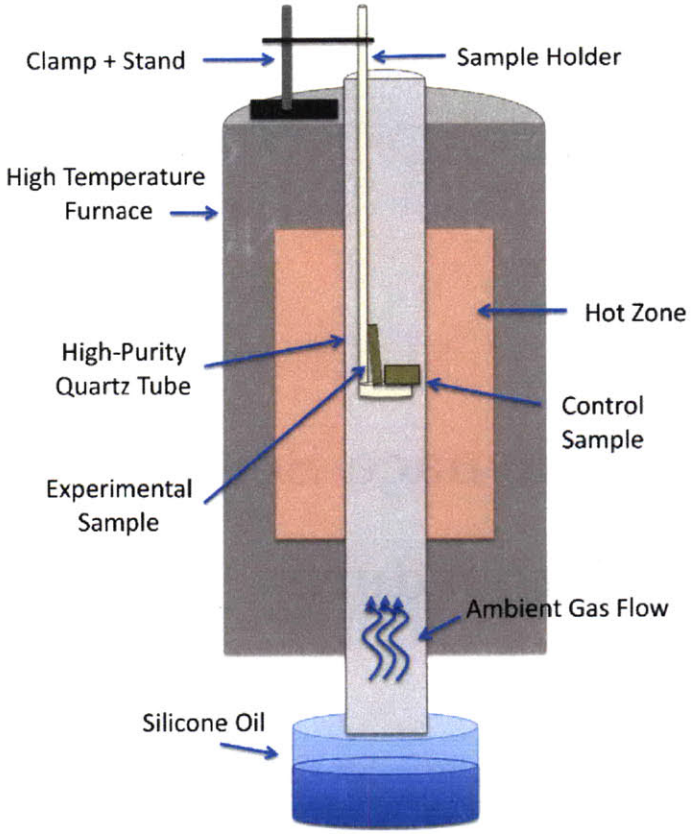

Figure 4-1: Schematic cross-section of Carbolite furnace setup in vertical orientation for quenching. The sample is suspended on a quartz holder within the hot zone of the furnace. A significant vibration of the sample holder drops the sample into the quenching fluid, normally silicone oil. Ambient gas flows into the furnace tube through the bottom.

4.2 Ambient Control

Samples for metal contamination by in-diffused were annealed in a forming gas atmosphere to prevent oxidation. The gas contained 7% H_2/93% Ar. While forming gas is nominally a flammable gas, generally combustion cannot propagate following ignition because of the shielding inert gas. However, the gas tank is removed from proximity to the high temperature area for safety. The flow was established in the furnace for 5 minutes prior to introducing the samples by introducing the gas at the bottom of the furnace. The bottom of the furnace was sealed with an endcap to isolate the furnace environment. The endcap also provides a via for flowing the forming gas. The forming gas flow is introduced at the bottom of the furnace because if the gas

flows in from the top, the downwards forced convective flow would compete with the upwards, natural convective flow. With forming gas flow from the top, regions within the tube remain not well-mixed with the forming gas, and the ambient environment of the sample is poorly controlled. The top of the furnace tube was open to the atmosphere but a steady upwards flow of gas was established and confirmed by the need to secure the exhaust gas duct firmly so that it did not oscillate in the stream of the upwards convection of gasses escaping the furnace tube. No flowmeter was used, but the pressure upstream of the final valve on the gas cylinder was set at 10 psi prior to opening the valve and the valve was opened until a steady flow was established with the pressure regulator reading 5 psi.

4.3 Short Temperature Calibration

To calibrate the set temperature of the furnace to the temperature within the tube near the sample, a short calibration experiment was conducted. Ambient gas was flowed into the tube for 5 minutes prior to taking a thermocouple reading at the set temperature. The results are shown in Fig. 4-2. The slope of the linear least-squares regression on the data, assuming a zero-intercept *i.e.* that the data passes through the origin, is 0.9755 with an R^2 coefficient of determination of 0.9795. The 95% confidence interval on the fitted slope is [0.9674, 0.9835].

4.4 Annealing Procedure

With the bottom end cap in place, the furnace was set to ramp to high temperature. The furnace was heated first from room temperature at 15°C/min to the Set Temperature (Set Temp) for Sample D, the highest temperature in the series. The ramp rate of the furnace is limited by the maximum thermal gradients that can be applied to the furnace tubes without causing excessive strain leading to premature failure. Once the set temperature was reached, the ambient gas flow was started and after a five minute setting period, the thermocouple (TC) reading was taken. An 18" type R

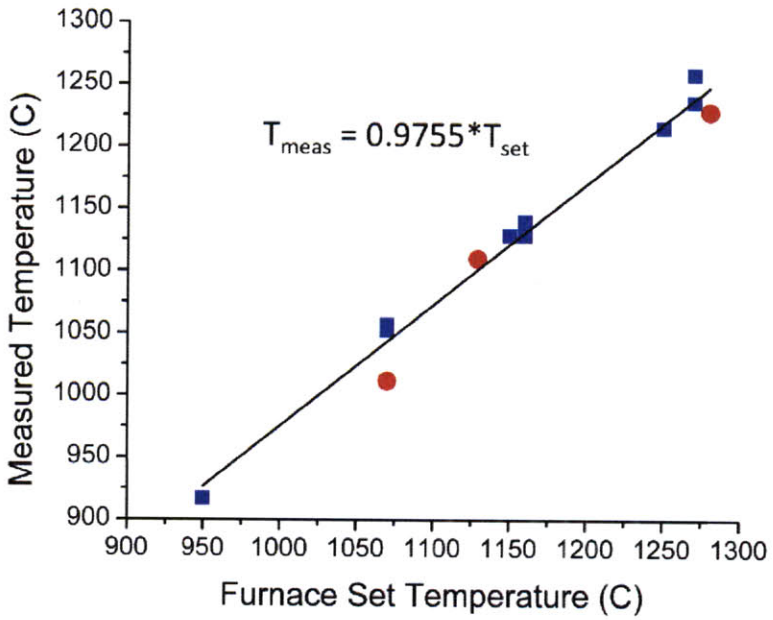

Figure 4-2: The temperature calibration line is shown in black. The red circles indicate the measured temperatures corresponding to the retrograde melting experimental samples. All data points were taken into account in the regression.

thermocouple, shown suspended into the hot zone of the furnace in Fig. 4-3, is used to provide temperature feedback of the hot zone temperature, since the set temperature of the furnace is measured outside the annealing tube. The sample was then loaded, and after 30 minutes at high temperature, the samples were quenched into silicone oil, with further procedural details given below. Then, the furnace was cooled at 50°C/min to the next lowest sample set temperature, *i.e.,* the order of anneals was: D, C, B, A. After a five minute settling time at the new set temperature, the next sample was loaded and the procedure repeated.

4.4.1 Loading A Sample

Loading a sample for a contamination anneal is often done with the furnace already at high temperature rather than ramping up from room temperature in order to precisely control the annealing time between samples at different temperatures. With the furnace often set to temperatures over 1000°C, extreme caution must obviously

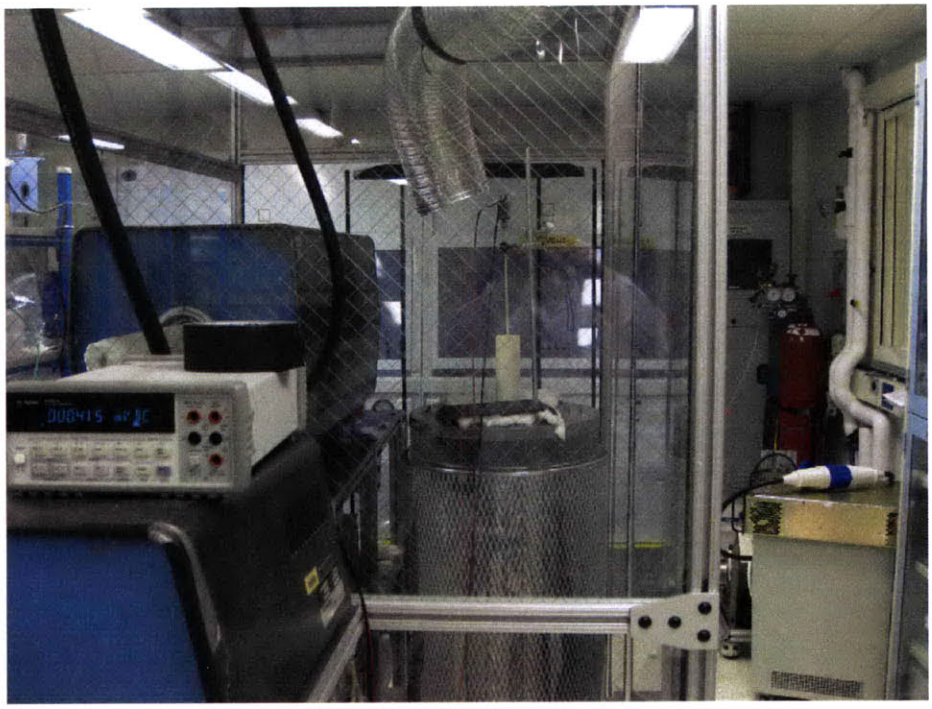

Figure 4-3: The additional temperature feedback Type-R thermocouple is shown here suspended into the furnace held by a lab clamp. Measurements are taken with the ambient gas flowing in order to account for the changing convective condition.

be taken.

Once the furnace reaches the set temperature of the anneal, the experimental and control samples are positioned on a quartz sample holder as shown in Fig. 4-1. The quartz holder is adjusted to the proper height so that the sample will be within the hot zone of the furnace using a standard lab clamp and clamp stand. Then the entire unit of the quartz holder + lab clamp is *carefully* lifted into place above the furnace tube and slowly lowered into position such that the lab stand rests on the top of the furnace with the sample in the hot zone. After lowering the clamp stand into place, I verify that the sample has not fallen from the sample holder during the loading process by using a mirror to look at the sample down the furnace tube. The view looking down the furnace tube at a sample at high temperature is shown in Fig. 4-4.

Figure 4-4: A view of the silicon sample on the quartz sample holder in the hot zone of the furnace is shown looking down the annealing tube. Photo courtesy of B. Newman.

4.4.2 Quenching

As for loading of a sample, because of the very high temperatures involved, quenching must be done carefully and with high-temperature gloves. Once the annealing time has expired, the endcap of the furnace is removed. As soon as the end cap is removed, the control over the ambient is lost and the samples must be quickly quenched to avoid oxidation which can occur within seconds. The samples are quenched by lifting the sample stand and firmly, but with very small amplitude, shaking the samples off the sample holder. To overcome the time period where ambient control is lost, a new generation of furnace tubes were designed for future quenching experiments. Their design is displayed in part drawings in Appendix A.

To load the next sample after quenching, the sample holder and clamp stand must be removed from the furnace and allowed to cool. A face shield is worn while the sample holder is extracted as slowly as possible from the furnace. Because of the small thermal mass, the sample holder cools quite quickly in ambient air.

Chapter 5

In-situ Annealing Setup at the Synchrotron

The technological cornerstone of the retrograde melting experiment is a modified Linkam TS 1500 hot stage designed for *in-situ* high temperature experimentation, shown in Fig. 5-1. Hudelson customized the stage in order to be able to mount it and acquire data at beamlines 10.3.2 at the Advanced Light Source at Lawrence Berkeley National Lab and at beamline 2-ID-D at the Advanced Photon Source and obtained results showing the first direct observation of retrograde melting in Si [49, 63]. The temperature-controlled, water-cooled stage is capable of elevating a sample 7 mm in diameter to temperatures of up to 1500°C in a controlled atmosphere with ramp rates of 1-200°C/min [64].

Among the technological adaptations of the stage for the X-ray experiment are the use of a X-ray transparent window and a clamp to secure the sample in the vertical orientation required by the beamline. A small piece of Ti is attached to the clamp near where it contacts the sample to act as an oxygen getter to prevent oxidation of the sample at high temperatures. The requirements and experimental accommodations for the window and clamp are discussed below, along with a discussion of the synchrotron experimental techniques and procedure.

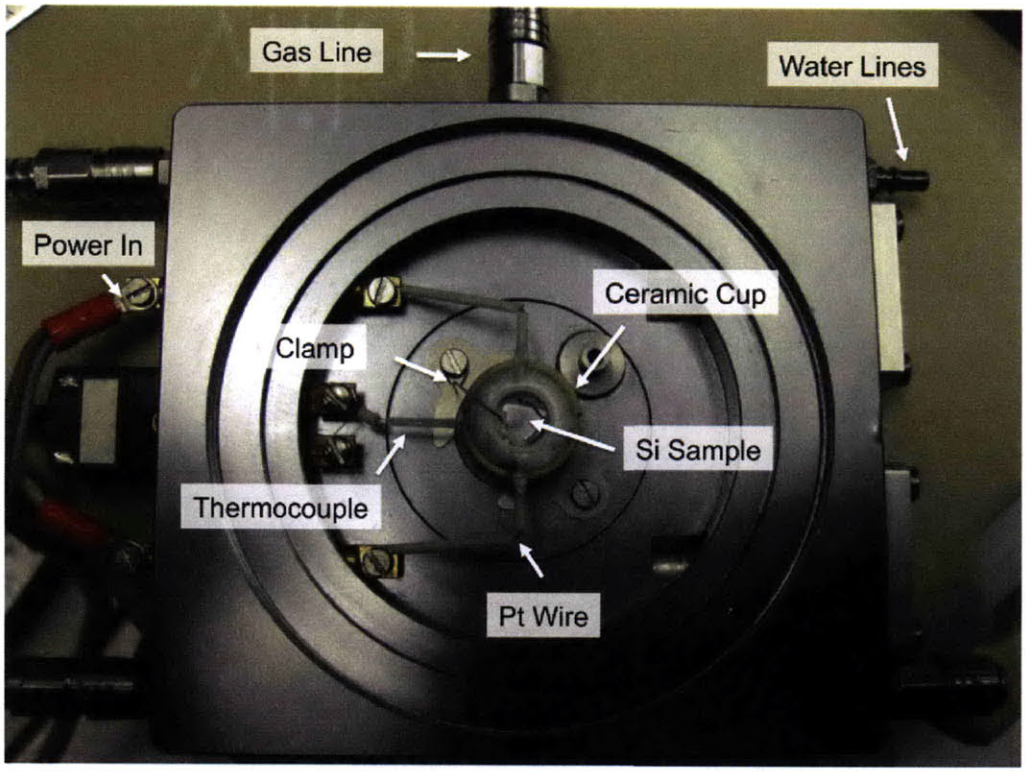

Figure 5-1: A view of the hot stage. Figure adapted from [63].

5.1 X-ray window materials

An X-ray transparent window is required to isolate the experimental volume and maintain atmospheric control of the high-temperature *in-situ* experiment. Because both the incoming and outgoing X-ray radiation must pass through the window, it is important that the window be highly X-ray transparent in the range of energies of interest. The beamline geometry at ALS 10.3.2 with the hot stage in place is such that the sample normal is angled with respect to the incident beam with angle $\alpha = 35°$ and with respect to the detector with angle $\beta = 55°$ as represented schematically in Fig. 5-2. The incoming beam and outgoing signal are attenuated by the solid window. Transmission due to a window with thickness, t, is according to Beer-Lambert's law:

$$I = I_o \cdot \exp\left(-\frac{t}{\lambda_{in} \cdot cos\alpha} - \frac{t}{\lambda_{out} \cdot cos\beta}\right) \tag{5.1}$$

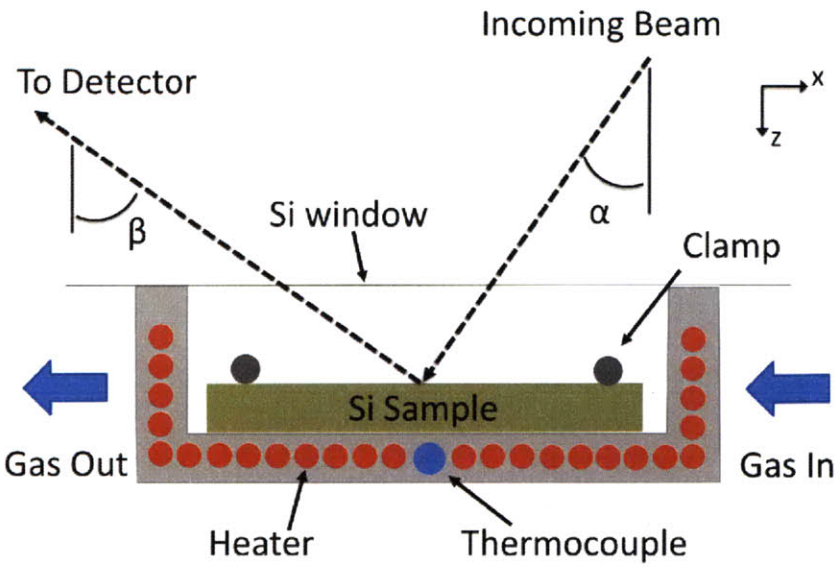

Figure 5-2: A cross-sectional drawing of the hot stage setup used for *in-situ* experimentation at beamline 10.3.2 at the ALS is shown here. The window and the gas lines provide ambient control, while the thermocouple, heaters, and water-cooling system (not shown) provide thermal control. Image adapted from [63].

where I and I_o are the outgoing and incoming intensities, and λ_{in} and λ_{out} are the characteristic attenuation lengths of the incoming and outgoing X-rays in the window material. In reality, the observed transmission through a 15 +/- 5 μm Si window is significantly less than that predicted by Eq. 5.1 [63]. Therefore, ideally a more highly transparent, applicable material could be found. In addition, the thin Si wafers used to date have been sourced through Virginia Semiconductor and University Wafer at a cost of $>$ \$100/wafer, and due to their fragility last only several days of wear and tear at the beamline. Table 5.1 is a compilation using data from [65] of the characteristic attenuation lengths of 10 keV X-rays in a number of candidate materials for the window.

An important consideration is the purity of the materials in Table 5.1 that is practially obtainable. Because our experiments often focus on environmentally common contaminants (e.g. Fe, Ni, and Cu), many materials such as Be are rarely available

Table 5.1: Characteristic Attenuation Length of 10 keV X-rays

Material	**Attenuation Length (μm)**
Si	133.707
Si_3N_4	140.435
Al	149.608
SiO_2	252.136
BN	1787.93
C	2066.64
Mylar	2177.29
Polyimide	2348.04
PMMA	2656.74
Polycarbonate	3025.96
Parylene-N	4379.48
Polypropylene	5741.58
Be	9594.00

at levels of purity that will not inject noise into our measurements.

Another competing concern is that the window maintain mechanical strength and stability despite the repeated cycling to high temperatures and the slightly elevated pressure from the gas flow.

To test the ability of the high-transmission materials from Table 5.1 to withstand high temperatures, 1" windows were cut from aluminized mylar, polyimide, and aluminum sheet. Not included in the test were: polypropylene, PMMA, and polycarbonate, which being thermoplastic polymers, have low glass transition and melting temperatures, and parylene which has low resistance to oxidation at high temperatures. The test was conducted by heating the hot stage at 100°C/min until the window failed or until a reasonable experimental temperature was achieved, at which point the stage was held at temperature. Two trials with polyimide windows were conducted, one at a hot stage set temperature of 1300°C and the other at the more common experimental temperature of 1100°C. The results of these windows test are shown in Table 5.2. Unfortunately, only the Al sheet survived the high temperature test. Al, however, is insignificantly more transparent than Si and is only available with relatively high impurity levels. The survival of the Al sheet does indicate, though, that the window temperature is less than the melting temperature of aluminum (T_m = 660°C) even when the stage is at 1300°C.

Table 5.2: Test of Window Materials at High Temperature

Material	Thickness (in.)	Test Result	Comment
Al	0.010	Good	$\therefore T_{window} < 660°C$
Aluminized Mylar	0.002	Melted	$T_{stage} = 575°C$
Polyimide	0.001	Cracked	$T_{stage} = 1300°C$, 2 min.
Polyimide	0.001	Cracked	$T_{stage} = 1100°C$, 10 min.

None of the high-transparency candidate materials considered survived the test. However, the polyimide films survived intermediate temperatures. A one-sided aluminization of the polyimide film may allow for less radiative heat transfer to the window, lowering the steady-state temperature of the window to a range where the polyimide film remains stable. For now, we continue the use of thin-Si windows for *in-situ* experiments.

5.2 Sample Clamps and Temperature Calibration

At the synchrotron, the experimental sample is mounted in a vertical orientation so that its front surface is perpendicular to the horizontal incident beam. To use the *in-situ* hot stage, the sample must therefore be secured against the hot stage heating element with the whole apparatus mounted vertically. To date this has been accomplished through the use of a tungsten (W) wire (shown in Fig. 5-1), shaped to provide a clamping force that holds the sample against the bottom of the heating element cup. This arrangement, however, leads inevitably to the development of a significant interfacial thermal resistance as the sample is not in good thermal contact with the heating element. The non-negligible thermal resistance develops a temperature drop between the hot stage cup and the experimental sample.

5.2.1 Hot Stage Temperature Calibration Setup

To empirically adjust for the systematic difference between the stage set temperature (as measured by a thermocouple at the base of the sample cup) and the temperature of the sample, a hot stage calibration experiment was conducted. The typical

experimental setup is shown in Fig. 5-3. An optical pyrometer is used to measure

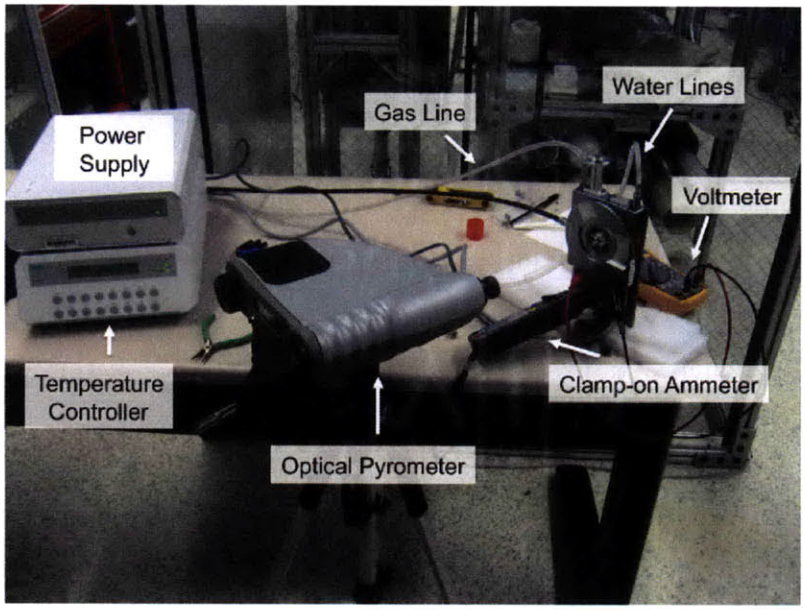

Figure 5-3: The typical setup for the hot stage calibration experiment is shown here. An optical pyrometer is used to measure the sample temperature, while a voltmeter and ammeter are used to measure the power delivered to the stage.

the sample temperature assuming an emissivity of silicon of $\epsilon = 0.63$ in the spectral and temperature range of the experiment [66]. A quartz window is mounted on the stage to control the atmosphere while maintaining optical transparency. To measure the power delivered to the stage in order to estimate the heat flow, a voltmeter is attached to the two electrodes, while a clamp-on ammeter is looped around the power delivery line. In this manner, the temperature of the sample, the set temperature of the stage, and the power in can be measured for a range of sample temperatures from $\approx$ 825 - 1350°C. Measurements in the lower end of the temperature range can only be achieved with little ambient light to allow for careful tuning of the optical pyrometer and so are best done at night with the lights off.

5.2.2 Hot Stage in Vertical Orientation

For the vertical orientation, a calibration curve, shown in Fig. 5-4 was developed assuming that each data point is an independent measurement using a least-squares linear regression. The resulting fit of the slope correlating the hot stage set temper-

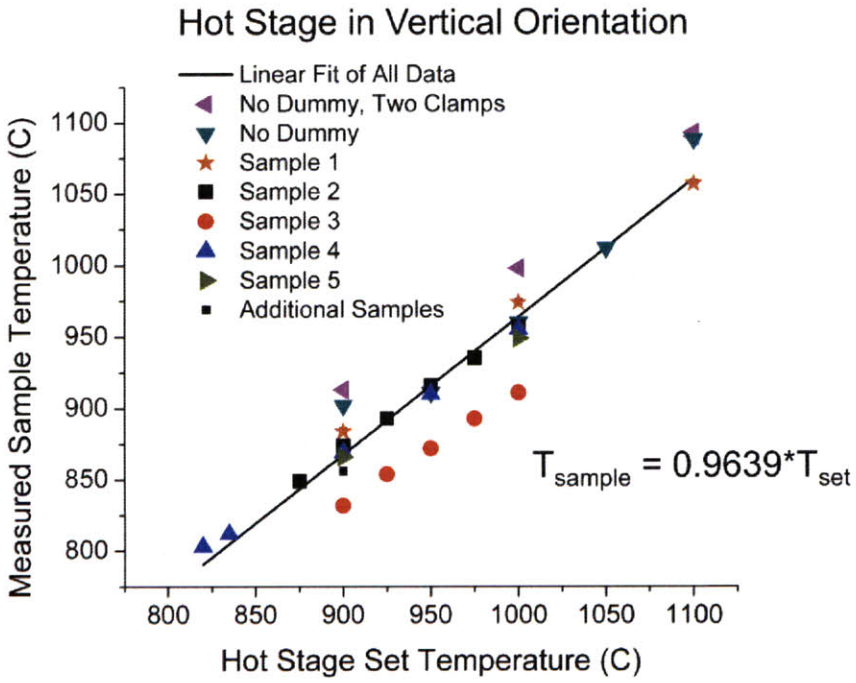

Figure 5-4: Hot stage calibration data in the vertical orientation are shown. The temperature of each sample was measured over a range of set temperature using the optical pyrometer. A least-squares regression fits the slope of the data.

ature to the sample temperature as measured by the optical pyrometer is:

$$T_{sample} = 0.9639 \cdot T_{set} \tag{5.2}$$

where the R^2 coefficient for the fit is 0.9035. The 95% confidence interval on the fitted slope of the calibration line is [0.9554, 0.9725].

It is important to note that much of the data are points taken sequentially for a given sample and so a relationship exists between data points that is not taken into account in the simple least-square regression that was carried out. Still, the data appear well fit by the linear regression model, such that the assumption that the data

points are all independent should have little effect on the outcome.

For Samples 1-5 in Fig. 5-4, the measurements were done with a dummy sample in place between the experimental sample and the hot stage cup to prevent excessive contamination of the hot stage cup with the impurities found in the experimental sample. The presence of the dummy sample appears to lead to a larger offset between the hot stage set temperature and the measured experimental sample temperature, indicating a larger thermal resistance which is likely a result of the addition of the interfacial thermal resistance between the dummy and the experimental sample, in addition to that between the dummy and the cup. Two samples, labeled "No Dummy" in Fig. 5-4, were tested without the presence of the dummy and fell in the upper range of the data. One of these no-dummy samples also was placed into contact with the cup with two W clamps rather than the single W clamp used for all the other samples. This "No Dummy, Two Clamps" sample exhibited the lowest difference between hot stage set temperature and measured sample temperature.

In addition to the simple calibration curve developed to predict the sample temperature from the set temperature of the stage, the current-voltage data can be used to assess the nature of the heat transfer. In Fig. 5-5, the power delivered to the stage, the current-voltage product, is plotted as a function of the temperature difference measured between the sample and the cup, effectively depicting the steady-state characteristic thermal resistance of each sample according to:

$$Q = \frac{\Delta T}{R_{eff}} \tag{5.3}$$

where Q is the heat transferred, approximated by the power delivered to the stage, ΔT is the temperature difference between the sample and the cup, and R_{eff} is the effective thermal resistance of the system.

While the data exhibit some scatter, each sample generally appears to have a constant thermal resistance, *i.e.* constant slope. Importantly, this relationship between power in or heat flow and the temperature difference does appear to be linear, meaning that conduction and/or convection dominate the heat transfer, rather than

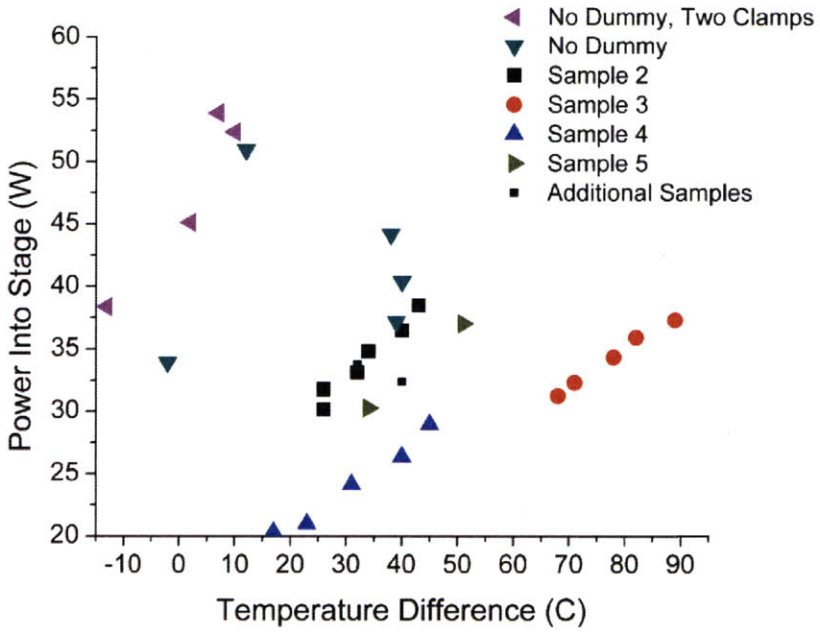

Figure 5-5: For the hot stage in the vertical orientation, the relationship between temperature drop between the hot stage cup and the sample is roughly linear with power delivered to the stage indicating that the heat transfer is dominated by conduction or convection losses. Experimental samples with no dummy sample beneath show a higher slope, indicating a lower thermal resistance.

radiation which varies as the difference of T^4.

The characteristic thermal resistance also appears to vary rather significantly between samples. In particular, the "No Dummy" samples exhibit the smallest thermal resistance, showing a steep slope ($1/R_{eff}$) and little temperature difference developing even for high rates of heat transfer. In other words, the setup for the "No Dummy" samples does not insulate the cup as significantly as the other samples with dummies in place, and so to achieve the high set temperature, the stage must draw more power. Again, especially the sample placed into contact with the cup with two W wire clamps and no dummy sample placed between the experimental sample and the hot stage cup showed a smal thermal resistance.

5.2.3 Hot Stage in Horizontal Orientation

While *in-situ* experiments are conducted in the vertical orientation, samples can also be annealed within the hot stage and quenched into a silicone oil directly, without the need for the high-temperature laboratory furnace. This can be very convenient for preparing samples immediately before synchrotron measurements. In this case, the hot stage is positioned resting horizontally until the allotted annealing time is reached, at which point the stage is rapidly flipped over, quenching the sample into liquid. By repeated measurement of the sample temperature with the optical pyrometer, a calibration line has been established for the hot stage when used in a horizontal configuration, shown in Fig. 5-6. For the horizontal configuration, a regression line

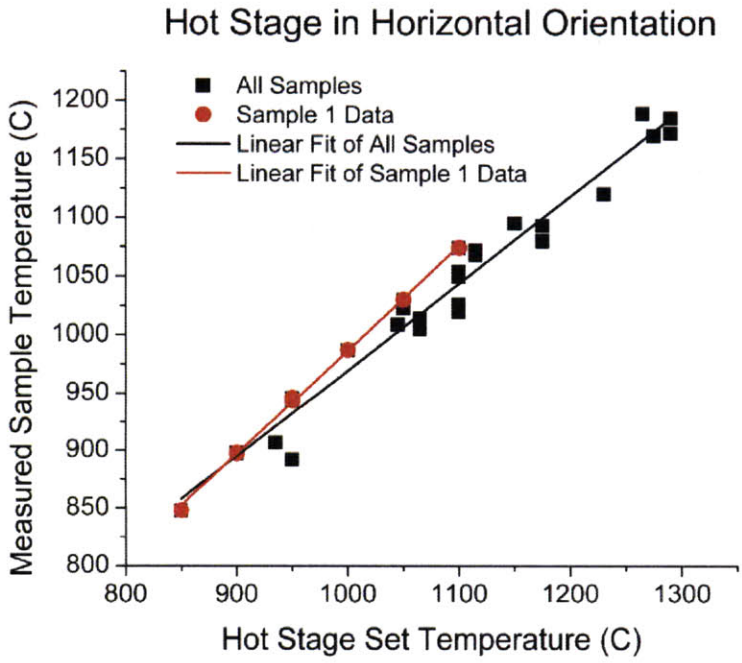

Figure 5-6: The hot stage calibration data for samples annealed in the horizontal orientation. All data points in black are independent measurements with a new sample each time, while the data in red are a single sample.

through the origin resulted in a poor fit of the data, unlike in the case of vertical orientation. Instead, the intercept was allowed to float as a second parameter of the

linear regression. The resulting least-squares fit was:

$$T_{sample} = 0.7428 \cdot T_{set} + 226.53 \tag{5.4}$$

The R^2 coefficient of determination for this regression was 0.9647. However, notice the large offset on the intercept required. The resulting uncertainty in the intercept value yields a rather large range for the 95% confidence intervals on the slope and intercept values of [0.6897, .7989] and [165.45, 287.613] respectively. These values represent a confidence interval on the values of the coefficients themselves and not on the prediction of the sample temperature.

One sample was measured over a range of temperatures, as it was not part of the broader experiment consisting of independently measured data points. For this sample, labeled Sample 1 in Fig. 5-6, the best fit was obtained by:

$$T_{sample} = 0.8946 \cdot T_{set} + 91.808 \tag{5.5}$$

which yielded a R^2 coefficient of 0.9989.

The incredible linearity for a given sample over the temperature range indicates that if a calibration curve for that an individual sample could be established by two or three points *in-situ*, then the rest of the temperature data could be considered calibrated to a high degree of accuracy. However, the *in-situ* X-ray experiment is inherently incongruent with a manual optical measurement, particularly because most X-ray transparent materials are not optically transparent in visible wavelengths (particularly the currently used Si).

One possible avenue for *in-situ*, simultaneous sample temperature measurement to avoid the problem of the varying contact resistance is to develop a two-color infrared (IR) pyrometer for measuring the sample temperature. Silicon is largely transparent to IR light, and so IR radiation from the sample will largely pass through the Si window. A two-color pyrometer removes the effect of the small transmission loss due to the window because by measuring the radiative energy at two wav'elengths, the temperature of the sample can be accurately characterized by the ratio of the

two energies measured rather than by their absolute values which are affected by the presence of the window.

5.3 Synchrotron Experimental Techniques

With the description of the hot stage and its modifications complete, I now turn to a description of the experimental techniques we used in the retrograde melting experiment. Beamline 10.3.2 is a bending magnet beamline that uses two Kirkpatrick-Baez mirrors to image a virtual source of varying size on the sample over a 3-17 keV energy range [67]. A 2 μm spot size can be achieved. The beamline is particularly well-suited for large-area X-ray fluorescence (XRF) scans to determine elemental distributions and regions of interest (ROIs), followed by X-ray absorption microspectroscopy to determine chemical state.

5.3.1 X-ray Microfluorescence

In X-ray microfluorescence, an incident beam of X-ray photons excites core shell electrons within a sample by providing an energy greater than the electron binding energy. The removal of a core shell electron leaves the atom electronically unstable, and an electron from a higher energy orbital will relax into the unoccupied, inner shell. The change in energy of the relaxing electron produces a secondary X-ray photon with an energy equal to the energy difference between the outer and inner orbitals, which is highly specific to every atom. By measuring the energy of the outgoing, secondary X-ray photon we can determine which element was excited.

Using a very bright X-ray source, like those of third-generation synchrotrons such as the ALS, we are able to focus the incoming X-ray beam down to small spot sizes while maintaining enough photon flux to produce a detectable number of secondary X-ray photons despite the high losses of X-ray optics. Mounting the sample onto a 2D sample stage allows us to raster the incident beam across the sample by moving the sample in the plane perpendicular to the beam. We thereby are able to produce elemental maps of large areas scans (up to square millimeters) with high resolution

(down to $\approx 2\,\mu m$) and high sensitivity ($> 10^{14}$ atoms/cm^2/sec) [30]. By measuring NIST calibrated XRF standards 1832 and 1833 in the same detector geometry as our experimental samples, we can also quantify the concentrations of metals within our samples.

5.3.2 X-ray Absorption Spectroscopy

While XRF can provide us information regarding the distribution and concentration of metal impurities in our silicon samples, X-ray absorption spectroscopy (XAS) can give us detailed information regarding the chemical state of the metals.

Whereas XRF involves probing the sample with a constant energy X-ray beam and scanning spatially, XAS involves holding fixed the position of the sample on a ROI and scanning in energy near the binding energy of the element of interest. Scanning in energy across the absorption edge results in the absorption of incoming photons increasing dramatically at the edge energy. The onset of the absorption edge can be changed, however, according to the chemical state of the atom. For example, if the atom is oxidized then the remaining electrons are generally bound more tightly to the nucleus and a higher energy is required to free them from the atom, and so the absorption edge will be measured to be a higher value than for the same atom in a neutral charge state.

Similarly, the identity and position of the nearest neighbors to the excited atom impact the absorption after the edge. Once the core electron has been excited, its wavefunction spreads radially from the excited atom and interacts with the neighboring atoms. This electronic interaction quantum mechanically affects the initial probability of excitation, such that a variation in absorption is observed as a function of energy due to the structural makeup of the neighborhood surrounding the excited atom. For example, a change in local environment of the excited atom from a silicide to an oxide can be observed accordingly.

In the retrograde melting experiment of this thesis, XAS measurements are used to determine the change in structure due to solidification of liquid precipitates into their solid phase upon cooling below the binary system's invariant point.

5.4 Local Melting Synchrotron Data Acquisition Procedure

The Ni-Si system was selected in part because of the large change in structure observed via XAS upon solidification of liquid droplets. The experiment was carried out at an energy 150 eV above the Ni K_α edge to maintain a high degree of sensitivity to Ni. The sample was heated within the hot stage in an Ar environment to avoid oxidation and the associated change of chemical state.

Each experimental sample was heated at 100°C/min. to the desired high temperature in an effort to proceed quickly and avoid sample oxidation. After observing complete dissolution of Ni using XRF, the sample was cooled 10-20°C at 100°C/min. until precipitation was seen. A 1 min. equilibration time was then given, holding temperature constant, after which a roughly 1.5 min. XRF scan with 10 μm steps, a 50 millisecond dwell time, and slit sizes of 200x30 mm was taken of the local area to find a large particle. Once a particle was located, 20 quick XAS (QXAS) of approximately 20 seconds each were taken using a slew scan of the monochromator across energy space to quickly reduce the white noise. Following the XAS measurements, the temperature was stepped down again and the cycle repeated until well below the observation of solidification.

The XAS standard sample was heated at 100°C/min to a stage set temperature of 1150°C whereupon high temperature XAS measurements were taken to confirm the liquid phase. The temperature was then stepped down 10-20°C and XAS measurements taken in the same manner as for the experimental samples, and the process repeated until well below the eutectic temperature.

Chapter 6

Retrograde Melting Experimental Results

A Note on Data Processing

XRF data processing was carried out using scripts I developed for MATLAB to normalize the data according to the incident beam flux and point by point dwell time. XAS measurements were deglitched using beamline 10.3.2 software developed by the beamline scientist [68], then calibrated, aligned, and normalized using the Athena data analysis program [69].

6.1 Ni Standard Sample Synchrotron Results

The first step of the experiment was to establish the QXAS spectra typical of the high-temperature liquid Ni-Si and the solid $NiSi_2$ phases using the standard sample with the Ni surface layer. While heating the standard sample from room temperature, XRF maps were taken to identify the ROI around the defect sites created by scratching the sample surface with a diamond scribe as described in Section 3.2. The low-"temperature XRF scan is shown in gray-scale depicting the number of Ni fluorescent counts per point in Fig. 6-1(a). The map was taken while heating so the temperature of the sample is varying along the height of the map, shown by the approximate

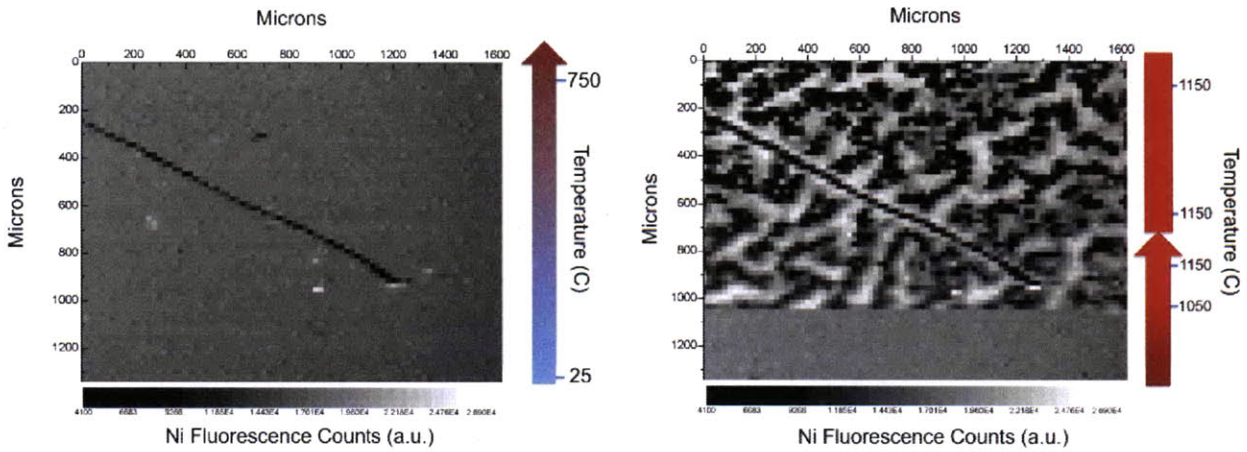

(a) From Room Temperature to ≈ 700°C

(b) From 750°C to 1150°C

Figure 6-1: The low temperature map of Ni fluorescent counts shows a uniform film, but the high temperature map shows the dewetting of this film as the surface layer transforms into liquid.

temperature bar to the right of Fig. 6-1(a). The Ni is evenly distributed across the surface of the sample, save for the scratch through the Ni layer. Upon heating above the eutectic temperature, the distribution of Ni in the XRF scan changes dramatically, however, as seen in Fig. 6-1(b). The temperatures shown are the set temperatures of the stage and so are higher than the actual temperature of the sample as discussed in Section 5.2.2. Still, we see evidence of liquefaction as the uniform film breaks up into concentrated islands of Ni as the eutectic is reached. This visible dewetting of the Ni film on the surface provides the first experimental confirmation of the phase transition to a liquid state.

To further confirm the phase transition and to acquire QXAS spectra of the liquid and solid phases of the precipitates, the sample was cooled according to the procedure discussed in Section 5.4. The spectrum corresponding to each temperature step as the sample was cooled is shown in Fig. 6-2 with a small vertical offset to allow direct comparison of the variation in the spectra with temperature. The XAS waterfall confirms the phase transition upon cooling from the high temperature liquid state to the solid $NiSi_2$. The temperatures associated with each spectra in Fig. 6-2 is the set temperature of the hot stage.

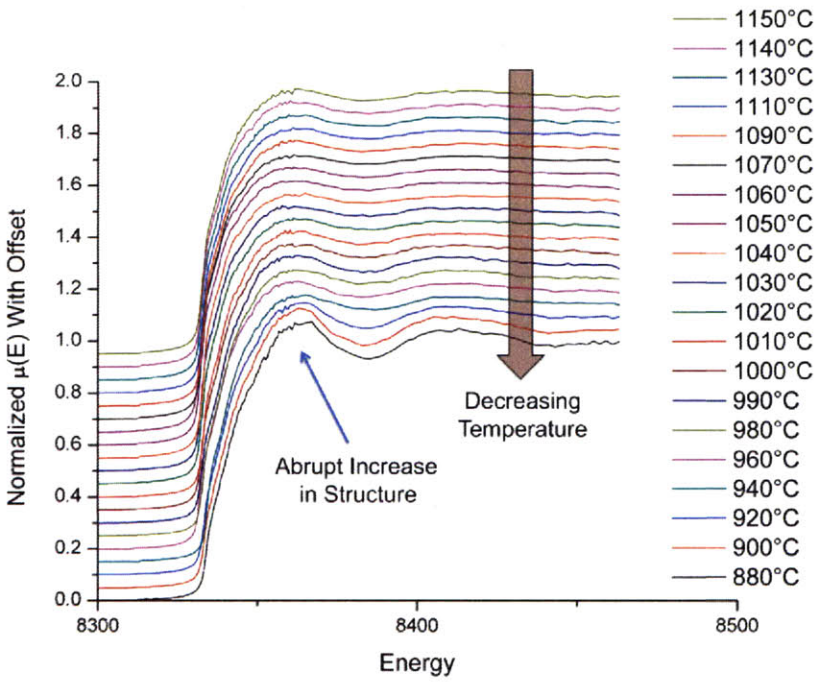

Figure 6-2: The normalized absorption spectra for the Ni standard sample are shown as a function of temperature with a vertical offset to allow for comparison of the spectra. As the temperature decreases well below the eutectic temperature, an abrupt change in structure is evidenced by the appearance of large beat patterns in the absorption data above the edge. Energy in eV.

In addition to fingerprinting the phase change in energy space, the spectra were converted into k-space which can more clearly show the structure present in the absorption measurement. The k-space measurements for the same spectra of the Ni standard sample are shown in Fig. 6-3. The lowest temperature scans, highlighted by the red box in Fig. 6-3, clearly show the development of structure indicating the transformation into a solid phase with a regularly repeating crystalline lattice.

Having established the expected liquid and solid spectra by fingerprinting the standard sample created by heating the evaporated Ni film on the Si substrate, I now turn to the analysis of the experimental samples which contain a solid state solution of Ni impurities in Si.

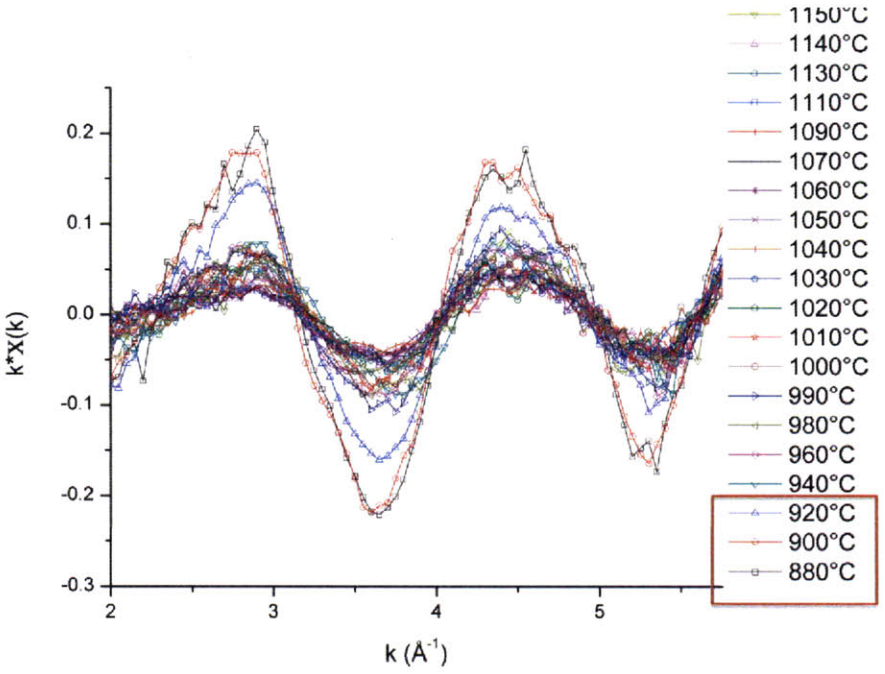

Figure 6-3: Converting the absorption spectra from energy space into k-space wth a k-weight of one clarifies the change in structure seen for the lowest-temperature spectra. The surface particles appear to solidify at a hot stage set temperature of 920°C.

6.2 Synchrotron Results for Experimental Samples

For the four experimental samples, the behavior upon heating is significantly different than for the standard sample, and it is helpful to review the XRF data to understand the interactions within the system. Then, after examining characteristic XRF data for Sample B as an example of the behavior of the experimental samples, the XAS measurements which distinguish the phase transition for each sample will be displayed.

6.2.1 XRF Maps: Diffusion, Segregation, and Precipitation upon Heating

The $NiSi_2$ lattice is closely lattice-matched to native Si, with less than a 0.4% change in lattice parameter from the diamond cubic structure of Si to the cubic CaF_2 structure of $NiSi_2$ [70]. The small volume change leads to extensive nickel precipitation within the bulk during quenching. Such small, localized clusters of Ni can be seen in the room temperature map of Sample B as single-pixel hotspots shown in Fig. 6-4(a), taken after the quench but prior to any further annealing.

The diffusivity of the Ni impurities atoms increases exponentially with temperature. Therefore, once heated above several hundred °C, any remaining supersaturated interstitial atoms have enough thermal energy to diffuse to the nearest heterogeneous nucleation sites and precipitate. Almost any surface defect provides a suitable nucleation site and precipitation occurs extensively as seen in Fig. 6-4(b), which is on the same color scale as Fig. 6-4(a).

However, once the temperature at which the contamination anneal and quench was performed is surpassed, the solid solubility of the Si wafer exceeds the total nickel concentration, and the particles dissolve as seen in Fig. 6-4(c). The complete dissolution of precipitates in Fig. 6-4(c) is in dramatic contrast with Fig. 6-4(b).

After all the nickel has returned to the dissolved state, we slowly cool the sample forcing supersaturation once again, but at a slower cooling rate the driving force for nucleation does not build as quickly and so only select sites provide a low enough energy barrier to nucleation to serve for heterogeneous nucleation. Then, the intentional scratching of the sample surface serves as the favored site for precipitation as seen in Fig. 6-4(d).

Once enough Ni has precipitated to take a XAS measurement without too much noise (roughly 10^4 cts/sec), we begin the stepwise cooling of the sample as described in Section 5.4, observing the chemical state at each temperature.

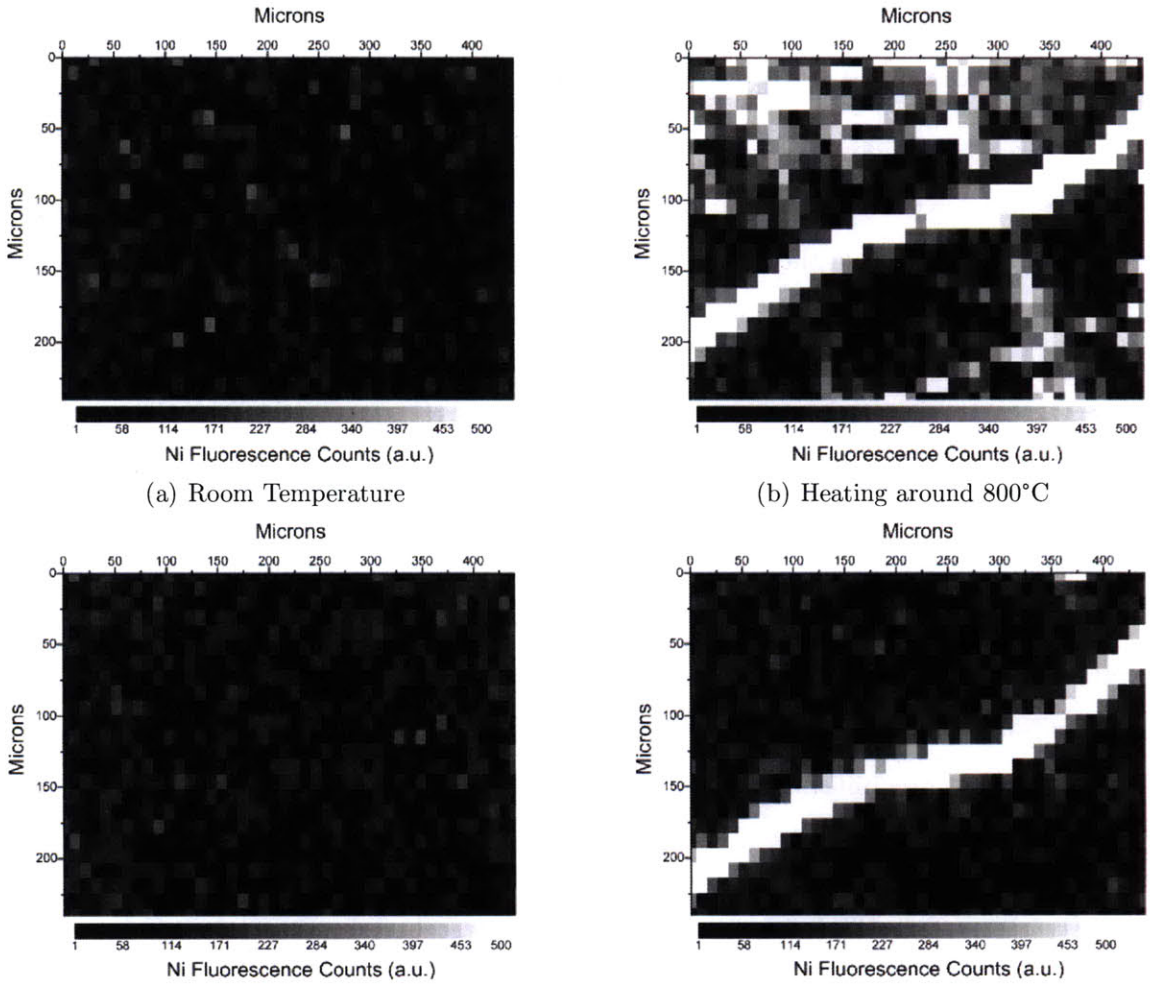

(a) Room Temperature

(b) Heating around 800°C

(c) Dissolved at 1200°C

(d) Retrograde Melting at Preferred Site

Figure 6-4: Example XRF Maps of Sample B showing the effect of temperature on the precipitation behavior of Ni. A high degree of segregation to a preferred nucleation sites is seen as the sample is cooled from high temperature in (d).

6.2.2 XAS Measurements for Determining Phase

For each sample, the XAS measurements taken as the temperature was lowered step by step neatly fall into two groups: a highly disordered high temperature phase with virtually no repeating crystalline structure and the lower temperature solid $NiSi_2$ phase. Figs. 6-5(a)-(d) show the XAS measurements as a function of temperature for each sample.

The data improve as the contamination temperature of the samples increases as expected, because the higher solid solubility at the higher contamination temperature

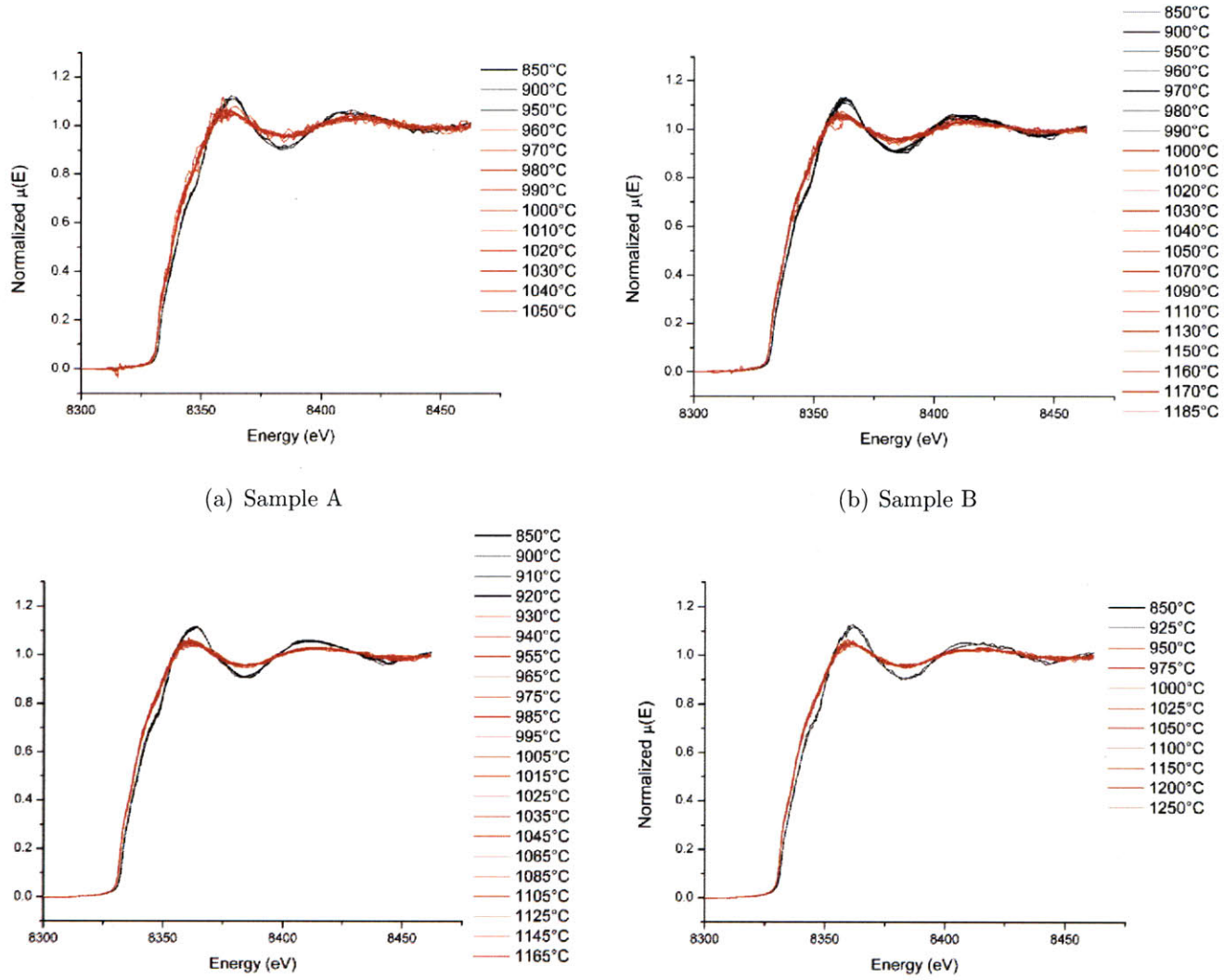

(a) Sample A

(b) Sample B

(c) Sample C

(d) Sample D

Figure 6-5: As with the Ni standard sample, the absorption spectra of the experimental samples fall neatly into two groups: a high-temperature state with high disorder indicating the liquid phase and the lower-temperature solid $NiSi_2$ phase.

allows for more atoms per precipitate and therefore a higher signal-to-noise ratio. Further evidence of the phase transformation can be seen in the spectra for samples A-D plotted in k-space in Appendix B. From the XRF and XAS data, it is clear that the data follow the expected retrograde melting mechanism whereby cooling from a saturated solution of Ni impurities in Si leads to precipitation of liquid droplets, followed by the solidification of the droplets into the $NiSi_2$ phase.

6.3 Single-Energy Temperature Scan

A separate attempt was made to distinguish the two phases by observing the change in absorption at a single energy as a function of temperature. Filipponi successfully used single-energy temperature scans to detect phase changes in Fe foils and Ge dispersed on BN and C substrates [71]. The idea of a single-energy temperature scan is to select an energy where the two phases differ significantly in absorption. Then, one can rapidly measure the temperature variation of the absorption with high temperature resolution compared to a normal energy scan because of the finite time per point in energy space required. For the Ni-Si energy space, 8360 and 8380 eV

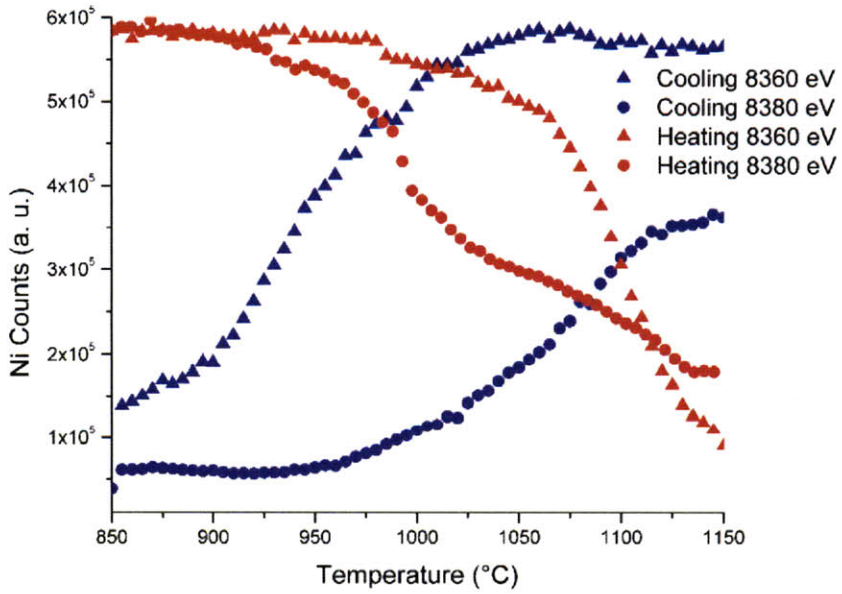

Figure 6-6: Single-energy temperatures scans at 8360 and 8380 eV. Absorption data are shown for heating and cooling ramps from 850 to 1150°C with a resolution of 3°C per point.

– corresponding to the peak and trough of absorption in the first "hump" in the XAS structure of the $NiSi_2$ phase – were chosen as two energies where the change in absorption is significant. Three second multi-channel analyzer (MCA) spectra were collected continuously, totalling all the counts of Ni observed within that time,

while the temperature was ramped 60°C/min, yielding a temperature resolution of 3°C/point. A particle was optimized for counts prior to each heating or cooling step. The results of the temperature scans at 8360 and 8380 eV are shown in Fig. 6-6.

Unfortunately, there is no clear trend of absorption with temperature. Instead, it appears that the particles drifted out of the beam spot during the temperature scan of 300°C due to thermal expansion and contraction. Thus, it would appear that such rapid temperature scans are not feasible for quality data for such small particle sizes. However, if the temperature ramp were made less aggressive and a small auto-optimization XRF map recorded between each MCA, the technique might be applicable.

6.4 ICPMS Results

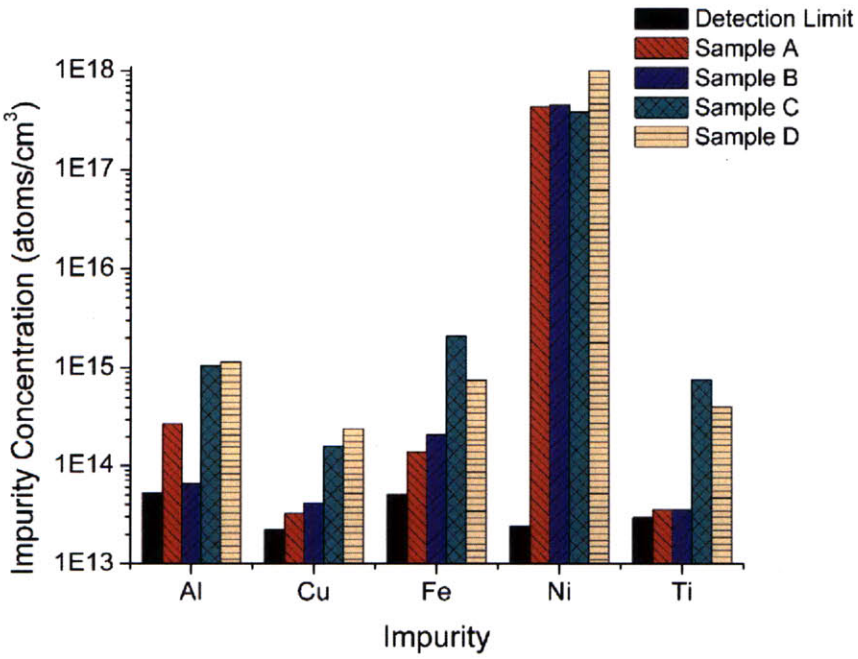

Figure 6-7: The ICPMS data resulting from analysis of control samples contaminated simultaneously with Samples A-D.

To confirm that the quenching and contamination of the experimental samples A-D proceeded as expected, we sent their twin control samples (see Section 3.2) out

for ICP-MS analysis. A 1 μm subsurface etch was performed to remove any surface contamination immediately prior to conducting the mass spectroscopy. Al, Cu, Fe, Ni, and Ti concentrations within the Si bulk were analyzed. Results of the measurement are shown in Fig. 6-7.

Relatively low concentrations of Al, Cu, Fe, and Ti compared to Ni were measured as expected, although the higher temperature samples appear to have incorporated significant concentrations from the diffusion furnace environment since the concentrations of unintentional contamination generally increases with temperature.

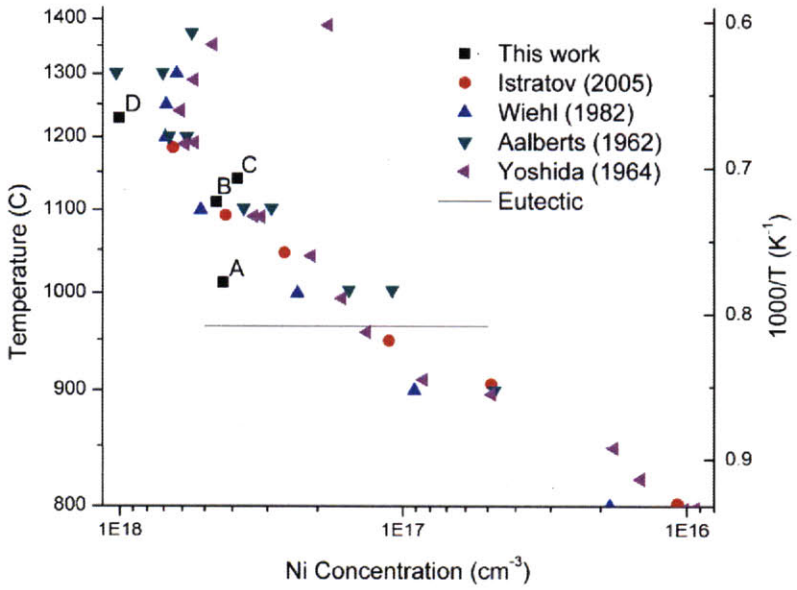

Figure 6-8: A compilation of literature data on the solid solubility of Ni in Si is shown for comparison with the ICPMS results from this work. The ICPMS results fit poorly with the existing literature.

To inspect the Ni concentration data further, the Ni data for Samples A-D are plotted in Fig. 6-8 along the Si-rich edge of the binary phase diagram along with solubility values from the literature [60, 72–74].

The temperatures used to locate the data on the ordinate were the temperatures measured with the thermocouple inside the annealing tube, as shown in Table 3.1. For Sample C, where no thermocouple measurement was taken, the calibration curve

for the furnace, shown in Fig. 4-2 was used to estimate the sample temperature during the anneal.

Unexpectedly, the Ni concentration measured by ICPMS does not increase monotonically for samples A-D as temperature increases. Instead, Sample C is measured to have a lower Ni concentration than either Sample A or B. Also, the concentrations measured for Sample A and B are almost equal despite the temperature difference of their contamination. Furthermore, Sample D is also measured to have an extraordinarily high level of Ni in solution, far above the solubility limits of the literature data at a similar temperature. In fact, only one other data point[72] has been measured to have a Ni solubility above 10^{18} atoms/cm^3.

Chapter 7

Discussion

7.1 Examining the Ni Retrograde Melting Data

Ultimately, the goal of this Ni retrograde melting experiment is to test the hypothesis that when a solution of Ni in Si supersaturates above the peritectic temperature, precipitation occurs in the form of localized liquid droplets. To this end, we would like to overlay a plot of the phase data from the XAS measurements versus temperature for the four experimental samples on the same axes as the solubility data from Fig. 6-8. For the ordinate, I will use the temperature calibration of the hot stage in the vertical orientation to convert from the stage temperatures shown for the XAS data in Fig. 6-5 to sample temperatures. However, the situation is less clear for the Ni concentration abscissa. Three options exist for displaying the Ni concentration of Samples A-D:

1. Use the ICPMS data taken on their twin samples

2. Locate the samples at the solubility limit from the literature data corresponding to the thermocouple temperature from the contamination anneal (Table 3.1)

3. Use the corresponding solubility limit from the literature data of the sample temperature at which all the Ni was observed to be dissolved at the synchrotron

Ideally, all three options would yield approximately the same values. However, the ICPMS data has significant inconsistencies as discussed above. Still, in Figs. 7-1-7-3, I plot the phase data versus temperature according to each of the three methods for locating the samples in concentration.

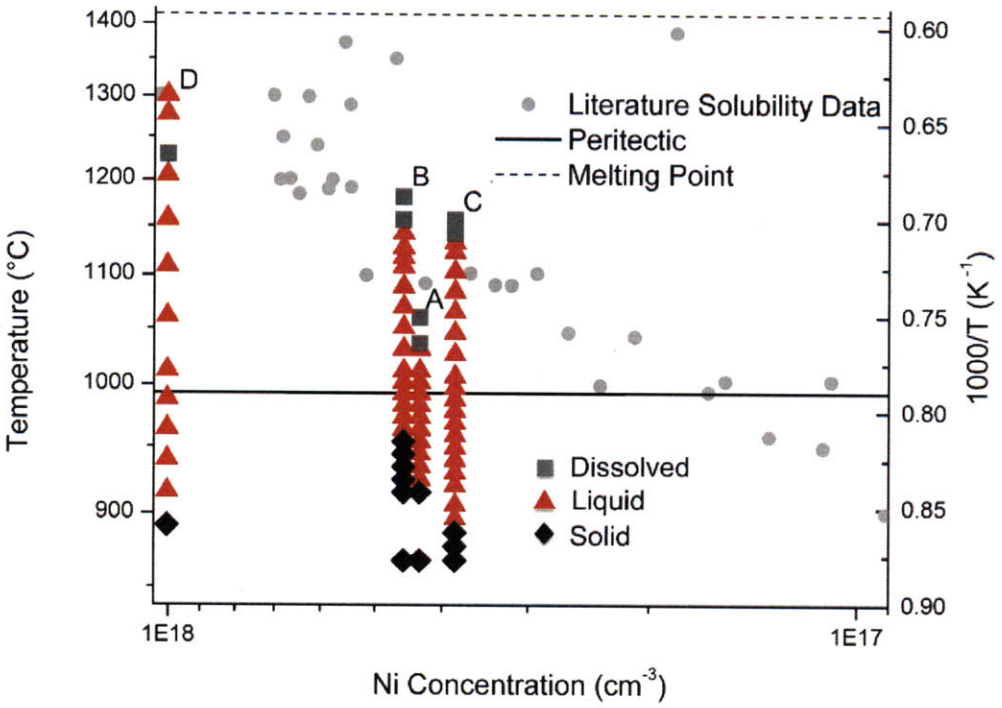

Figure 7-1: The phase as determined by XAS measurement is plotted versus temperature on top of the literature solubility data. The concentrations for each sample are as measured with ICPMS.

The data in Fig. 7-1 are muddled by the inconsistencies in the ICPMS data. While the trend of dissolution, followed by liquid precipitation, followed by solidification of precipitates with decreasing temperature is clear for each sample , the data are not coherent in concentration. Of particular note, Sample D exhibits a brief range of dissolution followed by a return to precipitation when the temperature was increased further. This increase in precipitation upon further heating demonstrates that Sample D contained an impurity concentration very near the maximum value for Ni in Si.

Plotting the XAS data versus temperature with the Ni concentrations corresponding to the thermocouple measurement of the contamination anneal, option(2), results in Fig. 7-2, where the data follow much clearer trends. Using the thermocouple data

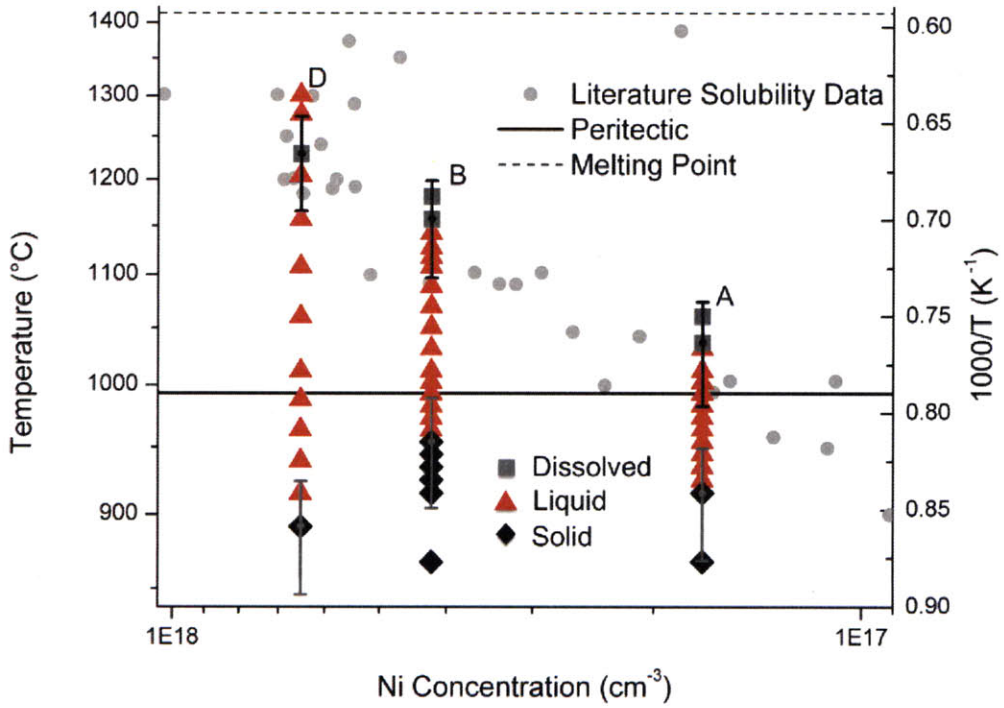

Figure 7-2: Again, the XAS phase data is plotted versus temperature. In this figure, concentrations for the experimental samples are taken as the solubility limit corresponding to the temperature measured by the thermocouple in the furnace during the contamination anneal. The bars do not represent the error in measurement of any individual point, but rather represent the maximum uncertainty in temperature for all data points due to the temperature calibration.

to locate the samples in Ni concentration, the measured dissolution and initial precipitation of the samples match the literature data within the scatter of the historical experiments. Sample D also falls near the peak of Ni solubility from the literature data, in good agreement with the XAS measurements. Unfortunately, no thermocouple measurement was taken for Sample C, and since the ICPMS measurement for that sample seemed particularly erroneous, we do not consider it further.

The bars shown in Fig. 7-2 for the dissolution and solidification temperatures of each sample represent the absolute limits on uncertainty of the temperature calibration, *i.e.* the temperature range shown by the bars is calculated using values for a calibration line that provide upper and lower bounds of all data points taken in the vertical orientation that are shown in Fig. 5-4. The bars are not the temperature error of each data point, but rather represent the largest possible shift in temperature that could be considered for all XAS measurements for that sample. Bars are shown for the dissolution and solidification temperature because the possible shift due to the maximum uncertainty in the calibration data is plotted on a nonlinear temperature scale in Fig. 7-2, and thus varies over the ordinate.

When choosing the sample concentrations according to the dissolution temperatures observed at the synchrotron, option (3), a very similar picture results, as shown in Fig. 7-3. From the similarity of option (2) with option (3), it is apparent that the dissolution temperatures observed at the synchrotron appear to agree well with the contamination temperatures, while the resulting datasets also match the literature data well. Within the uncertainty of the experiment, the samples exhibit retrograde melting upon supersaturation with no observed subcooling. Due to the variety of structural defects generated by scratching the samples surfaces, this lack of an energy barrier, which would cause subcooling of the supersaturated solution, is not surprising.

In all samples, however, an energy barrier for solidification of the liquid precipitates appears to cause subcooling of the liquid droplet as evidenced by the presence of liquid droplets below the peritectic temperature, even acounting for the uncertainty in temperature. As shown in Fig. 7-4, subcooling is also observed for the Ni standard sample. In the case of the standard sample with an evaporated film of Ni on the surface, because there is no shortage of Ni atoms at the Ni-Si interface during heating, it is assumed that the liquid takes on the eutectic composition, incorporating the requisite Si atoms from the near surface. During cooldown, the relevant invariant reaction is then the eutectic reaction.

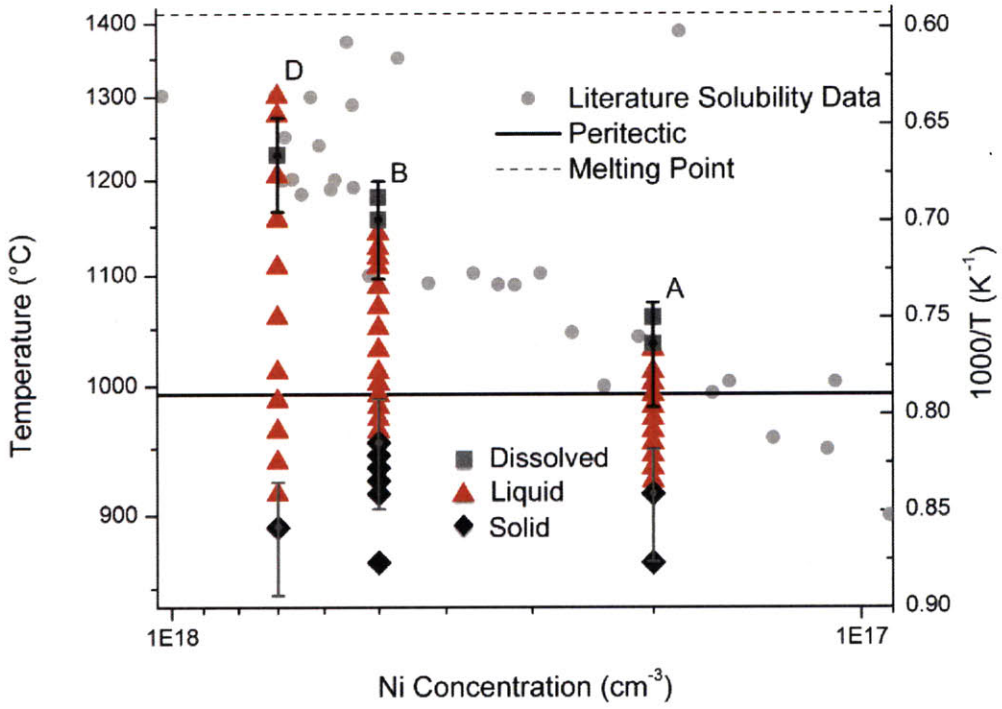

Figure 7-3: The XAS phase data are plotted versus temperature with the concentration of the experimental samples adjusted so that the dissolution temperature observed at the synchrotron corresponds to the solubility limits of the literature. Bars once again represent the maximum uncertainty for each sample.

In general, to transform a liquid Ni-Si droplet into $NiSi_2$, Si atoms must be absorbed into the precipitate to meet the stoichiometric 2:1 ratio of the solid phase, since the the peritectic concentration is 59% Si and the eutectic 56.2% [46]. To incorporate more Si into the precipitate, the energy to break existing Si-Si bonds is required. Furthermore, in the liquid phase, the surface energy term should be very small because of the high degree of disorder and the resulting lack of a rigid, crystalline lattice to generate interfacial strain. In contrast, for a solid precipitate, the lattice mismatch of $< 0.4\%$ for a $NiSi_2$ precipitate in Si, while small, causes a strain energy addition to the energy barrier.

Overall, the trend in the data and the mechanism of retrograde melting induced in silicon is clear: supersaturation of Ni impurities in the region of retrograde solubility

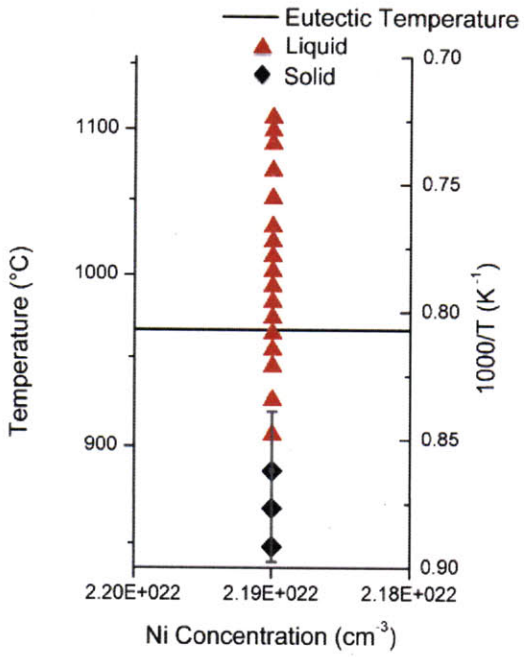

Figure 7-4: Subcooling is observed for the Ni standard sample as the liquid droplets remained stable well below the eutectic temperature of the system. Concentration displayed assuming the eutectic composition of 56.2% Si [46].

forces localized, microscopic formation of second-phase liquid particles.

7.2 Elemental Trends: Extending to Other Metal Systems

Given the successful prediction of retrograde melting in the Ni-Si binary system, we would like to survey the potential for retrograde melting to occur in other binary systems in Si.

A number of elements, including: Al, Ag, As, Au, B, Ba, Be, Bi, Ca, Cd, Ce, Co, Cr, Cu, Dy, Er, Fe, Ga, Gd, Hf, Ho, In, Ir, Li, Mg, Mn, Mo, Nb, Nd, Ni, Os, Pd, Pr, Pt, Pu, Rh, Ru, S, Sb, Sc, Se, Sn, Sr, Tb, Te, Th, Ti, U, V, W, Y, Zn, and Zr exhibit invariant reactions as the reaction in equilibrium with the boundary of the Si solid solution when cooling from the melting temperature of Si [46].

Of these, As, B, Ca, Cr, Mg, Mo, Sc, Ti, U, V, W, and Zr do not exhibit retrograde

solubility in Si and so would not undergo retrograde melting [11, 46, 56, 75].

The nature of the solvus line of: Ba, Be, Cd, Ce, Dy, Er, Gd, Hf, Ho, Ir, Nb, Nd, Os, Pd, Pr, Pt, Pu, Rh, Ru, Se, Sr, Tb, Te, Th, and Y in Si is not immediately available at high temperatures. Recently, the Si-Sr and Si-Ba phase diagrams have been analyzed over in the Si-rich region of the binary system [76], and hopefully more such investigations will follow shortly. However, for now, no conclusions can be drawn currently about the likelihood of retrograde melting occurring phenomenologically in these binary systems.

The remaining elements have been analyzed according to the properties of their phase diagram [11, 46, 56, 75] to calculate the driving force for nucleation of second-phase liquid particles according to:

$$f = kT \ln \left(\frac{c^{max}}{c^{eq}} \right) \tag{7.1}$$

which is the approximate precipitation driving force per impurity atom, as derived in Section 2.2, in a solution saturated at the maximum concentration of solid solubility of the impurity atom and then cooled to the invariant temperature (eutectic or peritectic). The driving force per atom of elements that are known to show retrograde solubility in Si are listed in Table 7.1. In this work, retrograde melting has been observed in the Ni-Si system. $NiSi_2$ has a particularly well-matched lattice in Si, and so nucleation energy barriers might be higher for other systems. However, systems with a similar or larger driving force per atom we would expect to precipitate out of solution in liquid droplets particularly along structural defects. Systems with a significantly smaller driving force are not expected to exhibit retrograde melting despite some degree of retrograde solubility. In summary, the potential for the elements to undergo retrograde melting in silicon has been displayed in Fig. 7-5.

Table 7.1: Approximate Driving Force for Retrograde Melting

Element	Driving Force (eV/atom)	Likely to Observe
Al	0.23	Yes
Ag	0.75	Yes
Au	1.01	Yes
Bi	1.10	Yes
Co	0.02	No
Cu	0.32	Yes
Fe	0.04	No
Ga	0.07	No
In	0.86	Yes
Li	0.03	No
Mn	0.16	Yes
Ni	**0.18**	Observed
S	0.08	No
Sb	0.07	No
Sn	0.15	Yes
Zn	1.16	Yes

7.3 Improving Minority Carrier Lifetime

For retrograde melting to occur, the system must be contaminated with an impurity concentration above the solid solubility of the impurity at its eutectic temperature in Si. Then, upon cooling of the system, precipitation will occur, and associated with precipitation in liquid phase there will be solid-to-liquid gettering, as seen in [49]. Judging from Fig. 7-5, a number of opportunities exist to incorporate retrograde melting into the refinement of silicon during the solidification of mc-Si casting.

Previously, Tang *et al.* [57] have studied the thermodynamic effect on the solid solubility and distribution coefficient of adding a third impurity element to binary Si systems during crystal growth and modeled a reduction in impurity content in certain systems. Experimentally, Yoshikawa and Morita have used retrograde solubility to reduce the B and P content of solar grade Si by growing crystals from an Si melt alloyed with Al and Ti based on the change in segregation coefficient [77–79].

In contrast to these studies, where retrograde solubility is employed to reduce the incorporation of impurities into the solid silicon ingot, retrograde melting could be employed to create liquid precipitation after the completion of the solidification

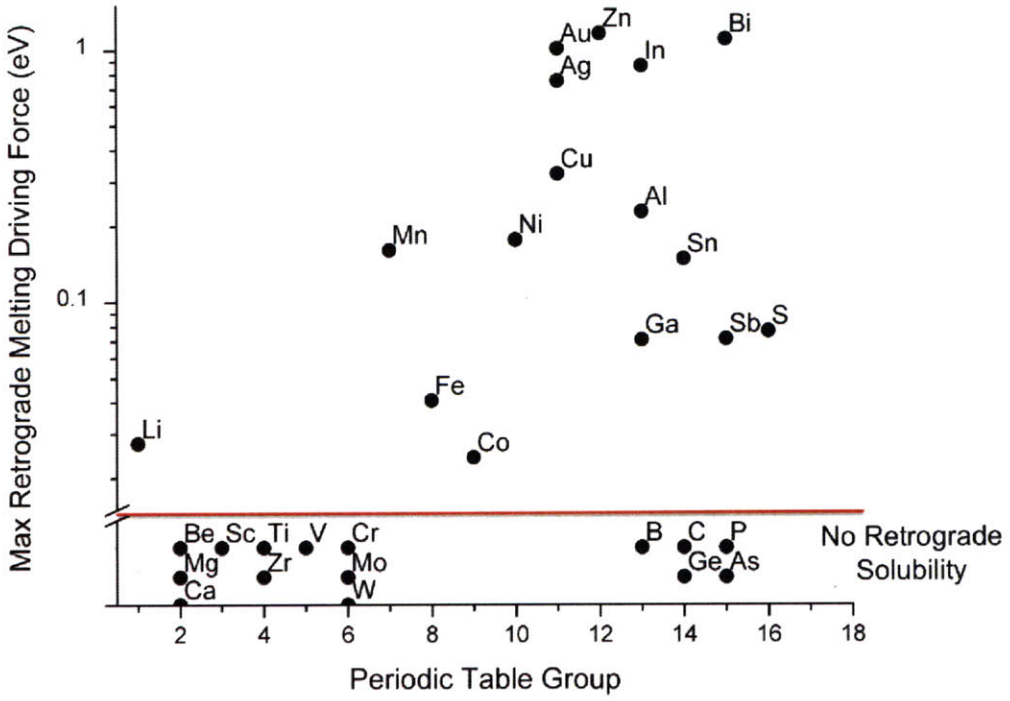

Figure 7-5: Following approximate calculations of the driving force for nucleation of liquid precipitates, tabulated in Table 7.1, the maximum driving force for retrograde melting is plotted with respect to position in the periodic table.

step. The liquid precipitates would then offer another opportunity for solid-to-liquid gettering. From Fig. 7-5, the primary candidates for retrograde melting include Au, Bi, In, and Zn which have very low eutectic temperatures in Si, 363°C, 271°C, 157°C, and 420°C respectively, and a low dissolved concentration at the eutectic such that low impurity concentrations would be required to form a liquid droplet. Al and Sn also have very low temperature eutectics (577°C and 232°C), but have very high solubilities requiring high contamination levels to activate the retrograde melting mechanism. Ag has a higher eutectic (835°C) but low solubility which could be effective. Cu, Mn, and Ni have intermediate eutectics (802°C, 993°C, and 1149°C) and relatively high solubilities and so may be less effective melting centers.

Moreover, the presence of multiple impurities, certainly the case in poor-'quality Si

feedstock materials, appears to suppress the system eutectic temperature [80], which would allow for an extended temperature range of solid-to-liquid gettering during a retrograde melting step.

For now, however, experimental confirmation of higher minority carrier lifetimes in conjunction with solid-to-liquid gettering activated by retrograde melting remains an open question.

Chapter 8

Conclusion

Retrograde melting is observed directly in the Ni-Si system using synchrotron-based X-ray techniques. The experimental observations match theoretical thermodynamic predictions and should allow for further modeling of impurity interactions during the crystallization cool down process. For photovoltaic applications using low-quality silicon feedstock, the potential for solid-to-liquid segregation via retrograde melting during cool down from crystallization may provide a pathway to impurity gettering and interstitial population reduction which could lead to as-grown lifetime improvements.

Appendices

Appendix A

Furnace Tube Drawings for Quenching Set-up

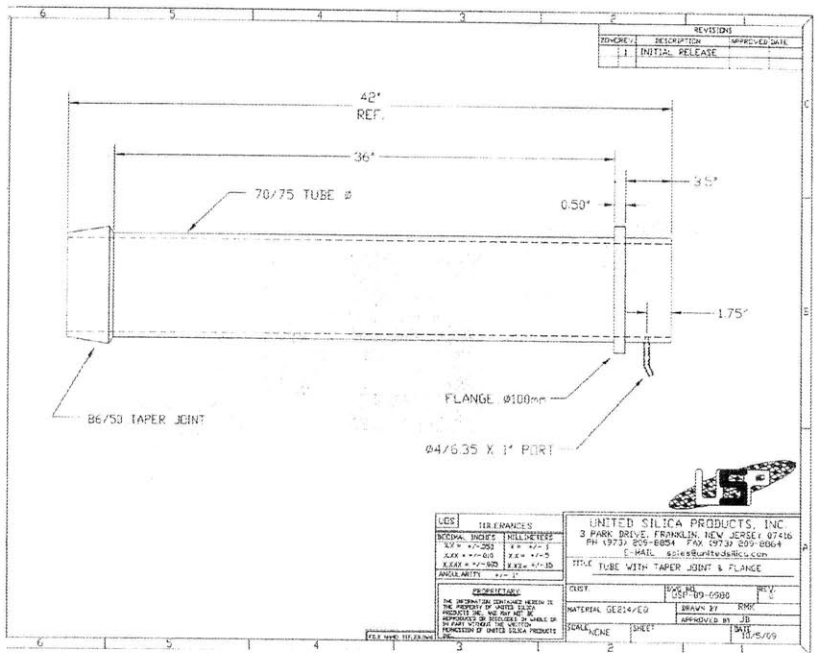

Figure A-1: Part drawing for the quartz tube used for high-temperature quenching. Note the inlet at the bottom for flowing ambient gas, even during the quench.

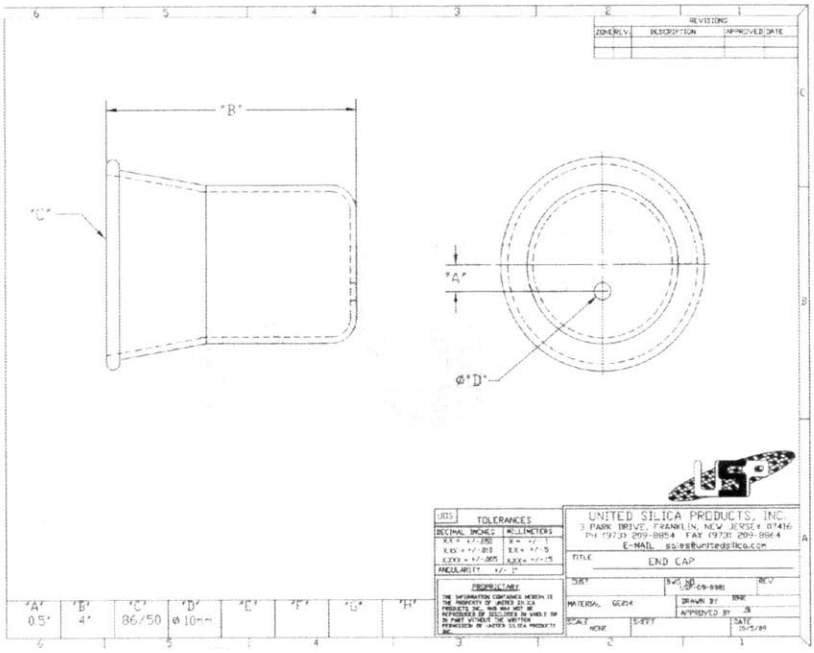

Figure A-2: Part drawings for the quartz tube end cap used for high-temperature quenching.

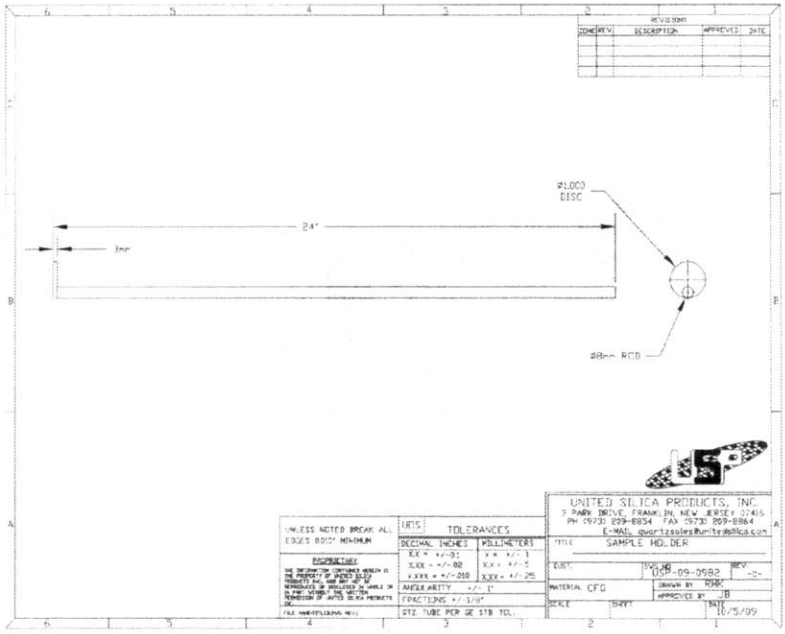

Figure A-3: Part drawing for the sample holder used for high-temperature quenching.

Appendix B

XAS Measurements for Experimental Samples Plotted in K-Space

For further comparison of the high and low temperature XAS measurements, I have plotted here the k-space spectra for the experimental samples.

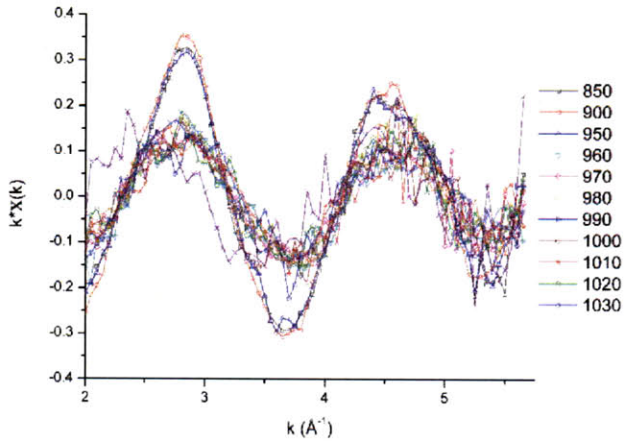

Figure B-1: Sample A XAS measurements transformed from energy space to k-space.

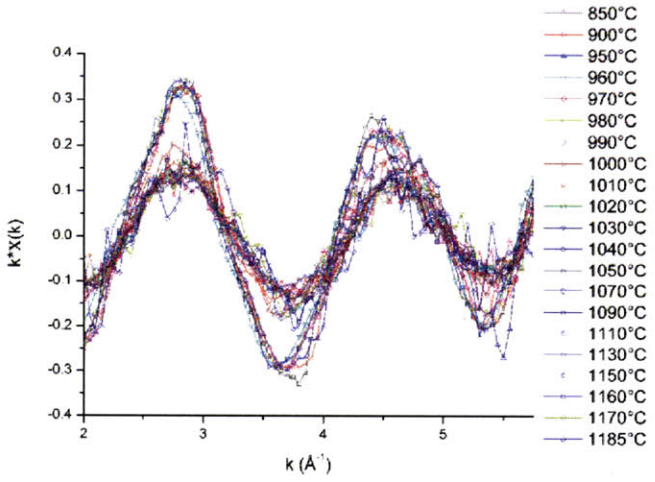

Figure B-2: Sample B XAS measurements transformed from energy space to k-space.

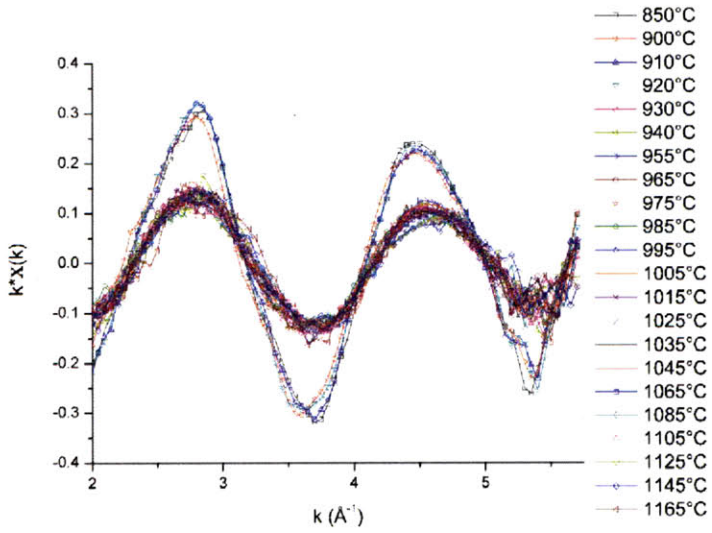

Figure B-3: Sample C XAS measurements transformed from energy space to k-space.

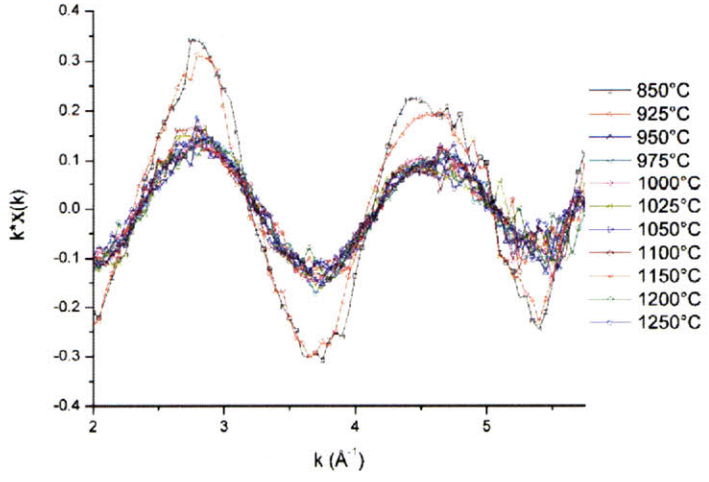

Figure B-4: Sample D XAS measurements transformed from energy space to k-space.

Bibliography

[1] Weston A Hermann. Quantifying global exergy resources. *Energy*, 31(12):1685–1702, Jan 2006.

[2] IEAPVPS. Trends in photovoltaic applications. *Report IEA-PVPS*, T1(18):1–44, Sep 2009.

[3] A Istratov, H Hieslmair, and E Weber. Iron contamination in silicon technology. *Applied Physics A: Materials Science & Processing*, Jan 2000.

[4] Gerardo L Araujo and Antonio Marti. Absolute limiting efficiencies for photovoltaic energy conversion. *Solar Energy Materials and Solar Cells*, 33(2):213–240, Jan 1994.

[5] C del Cañizo, G Del Coso, and W.C Sinke. Crystalline silicon solar module technology: Towards the 1 per watt-peak goal. *Prog. Photovolt: Res. Appl.*, 17(3):199–209, May 2009.

[6] RH Hopkins, R G Seidensticker, P Rai-Choudhury, PD Blais, and JR McCormick. Crystal growth considerations in the use of "solar grade" silicon. *Journal Of Crystal Growth*, 42(DEC):493–498, Jan 1977.

[7] R G Seidensticker and RH Hopkins. Silicon ribbon growth by the dendritic web process. *Journal Of Crystal Growth*, 50(1):221–235, Jan 1980.

[8] J Hofstetter, J Lelièvre, C del Cañizo, and A Luque. Acceptable contamination levels in solar grade silicon: From feedstock to solar cell. *Materials Science & Engineering B*, Jan 2008.

[9] G del Coso, C del Cañizo, and W C Sinke. The impact of silicon feedstock on the pv module cost. *Solar Energy Materials and Solar Cells*, 94(2):345–349, Dec 2010.

[10] JR Davis Jr, A Rohatgi, RH Hopkins, PD Blais, P Rai-Choudhury, JR McCormick, and HC Mollenkopf. Impurities in silicon solar cells. *IEEE Transactions on Electron Devices*, 27(4):677–687, 1980.

[11] ER Weber. Transition metals in silicon. *Applied Physics A: Materials Science & Processing*, 30(1):1–22, 1983.

[12] T Buonassisi, AA Istratov, M Heuer, MA Marcus, R Jonczyk, J Isenberg, B Lai, Z Cai, S Heald, and W Warta. Synchrotron-based investigations of the nature and impact of iron contamination in multicrystalline silicon solar cells. *Journal of Applied Physics*, 97:074901, 2005.

[13] HJ Queisser and EE Haller. Defects in semiconductors: Some fatal, some vital. *Science*, 281(5379):945, 1998.

[14] Daniel Macdonald and L. J Geerligs. Recombination activity of interstitial iron and other transition metal point defects in p- and n-type crystalline silicon. *Applied Physics Letters*, 85(18):4061, Jan 2004.

[15] W Shockley and W Read. Statistics of the recombinations of holes and electrons. *Physical Review*, 87(5):835–842, Jan 1952.

[16] D Macdonald and A Cuevas. Validity of simplified shockley-read-hall statistics for modeling carrier lifetimes in crystalline .... *Physical Review B*, 67(075203):1–7, Jan 2003.

[17] Tine Uberg Naerland, Lars Arnberg, and Arve Holt. Origin of the low carrier lifetime edge zone in multicrystalline pv silicon. *Prog. Photovolt: Res. Appl.*, 17(5):289–296, Aug 2009.

[18] R Kvande, L Geerligs, G Coletti, L Arnberg, and M Di .... Distribution of iron in multicrystalline silicon ingots. *Journal of Applied Physics*, 104(064905):1–9, Jan 2008.

[19] C del Canizo and A Luque. A comprehensive model for the gettering of lifetime-killing impurities in silicon. *J Electrochem Soc*, 147(7):2685–2692, Jan 2000.

[20] A Istratov, T Buonassisi, and R McDonald. Metal content of multicrystalline silicon for solar cells and its impact on minority carrier .... *Journal of Applied Physics*, Jan 2003.

[21] T Buonassisi, AA Istratov, MD Pickett, M Heuer, JP Kalejs, G Hahn, MA Marcus, B Lai, Z Cai, and SM Heald. Chemical natures and distributions of metal impurities in multicrystalline silicon materials. *Prog. Photovolt: Res. Appl.*, 14(6), 2006.

[22] Tonio Buonassisi, Andrei A Istratov, Matthew A Marcus, Barry Lai, Zhonghou Cai, Steven M Heald, and Eicke R Weber. Engineering metal-impurity nanodefects for low-cost solar cells. *Nat Mater*, 4(9):676 679, Sep 2005.

[23] T Buonassisi, A. A Istratov, S Peters, C Ballif, J Isenberg, S Riepe, W Warta, R Schindler, G Willeke, Z Cai, B Lai, and E. R Weber. Impact of metal silicide precipitate dissolution during rapid thermal processing of multicrystalline silicon solar cells. *Applied Physics Letters*, 87(12):121918, Jan 2005.

[24] S McHugo. Release of metal impurities from structural defects in polycrystalline silicon. *Applied Physics Letters*, Jan 1997.

[25] SA McHugo, AC Thompson, C Flink, ER Weber, G Lamble, B Gunion, A MacDowell, R Celestre, HA Padmore, and Z Hussain. Synchrotron-based impurity mapping. *Journal Of Crystal Growth*, 210(1-3):395–400, 2000.

[26] SA McHugo, AC Thompson, A Mohammed, G Lamble, I Perichaud, S Martinuzzi, M Werner, M Rinio, W Koch, and HU Hoefs. Nanometer-scale metal precipitates in multicrystalline silicon solar cells. *Journal of Applied Physics*, 89:4282, 2001.

[27] Tonio Buonassisi, Matthew A Marcus, Andrei A Istratov, Matthias Heuer, Theodore F Ciszek, Barry Lai, Zhonghou Cai, and Eicke R Weber. Analysis of copper-rich precipitates in silicon: Chemical state, gettering, and impact on multicrystalline silicon solar cell material. *Journal of Applied Physics*, 97(6):063503, Jan 2005.

[28] T Buonassisi, A. A Istratov, M. D Pickett, M. A Marcus, T. F Ciszek, and E. R Weber. Metal precipitation at grain boundaries in silicon: Dependence on grain boundary character and dislocation decoration. *Applied Physics Letters*, 89(4):042102, Jan 2006.

[29] OF Vyvenko, T Buonassisi, AA Istratov, H Hieslmair, AC Thompson, R Schindler, and ER Weber. X-ray beam induced current - a synchrotron radiation based technique for the in situ analysis of recombination properties and chemical nature of metal clusters in silicon. *Journal of Applied Physics*, 91(6):3614–3617, Jan 2002.

[30] T Buonassisi, AA Istratov, MA Marcus, M Heuer, MD Pickett, B Lai, Z Cai, SM Heald, and ER Weber. Local measurements of diffusion length and chemical character of metal clusters in multicrystalline silicon, Jan 2005.

[31] T Buonassisi, OF Vyvenko, AA Istratov, ER Weber, G Hahn, D Sontag, JP Rakotoniaina, O Breitenstein, J Isenberg, and R Schindler. Observation of transition metals at shunt locations in multicrystalline silicon solar cells. *Journal of Applied Physics*, 95(3):1556–1561, Jan 2004.

[32] Wolfram Kwapil, Paul Gundel, Martin C Schubert, Friedemann D Heinz, Wilhelm Warta, Eicke R Weber, Adolf Goetzberger, and Gema Martinez-Criado. Observation of metal precipitates at prebreakdown sites in multicrystalline silicon solar cells. *Applied Physics Letters*, 95(23):232113, Jan 2009.

[33] Robert Falster. Defect control in silicon crystal growth and wafer processing. *memc.com*, pages 1–12, Nov 2003.

[34] R Falster, D Gambaro, M Olmo, M Cornara, and H Korb. The engineering of silicon wafer material properties through vacancy concentration profile control

and the achievement of ideal oxygen precipitation behavior. *Materials Research Society Symposium Proceedings*, 510:27–35, Jun 1998.

[35] Shravan Kumar Chunduri. Bigger and better – and retro? *Photon International*, pages 1–23, Jul 2010.

[36] E Olsen and EJ Ovrelid. Silicon nitride coating and crucible-effects of using upgraded materials in the casting of multicrystalline silicon ingots. *Prog. Photovolt: Res. Appl.*, 16(2), 2008.

[37] A Haarahiltunen, H Savin, M Yli-Koski, H Talvitie, and J Sinkkonen. Modeling phosphorus diffusion gettering of iron in single crystal silicon. *J. Appl. Phys.*, 105(2):023510, Jan 2009.

[38] Mohammad B Shabani, T Yamashita, and E Morita. Study of gettering mechanisms in silicon: Competitive gettering between phosphorus diffusion gettering and other gettering sites. *Solid State Phenomena*, 131-133:399–404, 2008.

[39] D Macdonald, A Cuevas, and A Kinomura. Phosphorus gettering in multicrystalline silicon studied by neutron activation analysis. *29th IEEE PVSC*, Jan 2002.

[40] Daniel Macdonald and Andres Cuevas. The trade-off between phosphorus gettering and thermal degradation in multicrystalline silicon. *16th European Photovoltaic Solar Energy Conference*, pages 1–5, Jun 2000.

[41] H Adidharma, M Radosz, and M Luszczyk. Retrograde melting behavior in polyolefin plus solvent plus antisolvent solutions. *Aiche J*, 49(4):1044–1049, Jan 2003.

[42] DH Speidel and RH Nafziger. Retrograde melting in the system mg-fe-si-o. *Science*, 152(3727):1367–1368, 1966.

[43] S Wagner and D Rigney. Binary systems involving the reversible "catatectic" reaction solid i cooling to .... *Metall. Trans.*, Jan 1974.

[44] M Stier and M Rettenmayr. Microstructural evolution in near-metatectic cu-sn alloys. *Journal Of Crystal Growth*, 311(1):137–140, Jan 2008.

[45] R Ferro, A Saccone, S Delfino, AM Cardinale, and D Macciò. Inverse melting in binary systems: Morphology and microscopy of catatectic alloys. *Metallurgical and Materials Transactions B*, 27(6):979–986, 1996.

[46] Hiroaki Okamoto. *Desk Handbook: Phase Diagrams for Binary Alloys.* ASM International, 2000.

[47] T Buonassisi, M Heuer, A Istratov, M Pickett, M Marcus, B Lai, Z Cai, S Heald, and E Weber. Transition metal co-precipitation mechanisms in silicon. *Acta Materialia*, 55(18):6119–6126, Oct 2007.

[48] N Abrikosov and L Poretskaya. Investigation of the ternary sb-bi-te system. *Izv Akad Nauk SSSR Neorgan Materialy*, 1(4):503–510, 1965.

[49] Steve Hudelson, Bonna K Newman, Sarah Bernardis, David P Fenning, Mariana I Bertoni, Matthew A Marcus, Sirine C Fakra, Barry Lai, and Tonio Buonassisi. Retrograde melting and internal liquid gettering in silicon. *Advanced Materials*, in press, 2010.

[50] M Lindholm and B Sundman. A thermodynamic evaluation of the nickel-silicon system. *Metallurgical and Materials Transactions A*, Jan 1996.

[51] J Miettinen. Thermodynamic description of the cu-ni-si system in the copper-rich corner above 700 degrees c. *Calphad*, 29(3):212–221, Jan 2005.

[52] Asm international phase diagrams.. http://www1.asminternational.org/asmenterprise/apd/viewa

[53] CD Thurmond and JD Struthers. Equilibrium thermochemistry of solid and liquid alloys of germanium and of silicon .2. the retrograde solid solubilities of sb in ge, cu in ge, and cu in si. *J Phys Chem-Us*, 57(8):831–835, Jan 1953.

[54] Victor I Fistul. Impurities in semiconductors: Solubility, migration and interactions. pages 1–42, Dec 2003.

[55] Robert W. Balluffi, Samuel M. Allen, and W. Craig Carter. *Kinetics of Materials*. John Wiley And Sons, Inc., 2005.

[56] Takeshi Yoshikawa, Kazuki Morita, Sakiko Kawanishi, and Toshihiro Tanaka. Thermodynamics of impurity elements in solid silicon. *Journal of alloys and compounds*, 490(1-2):31–41, Jan 2010.

[57] Kai Tang, Eivind J Ovrelid, Gabriella Tranell, and Merete Tangstad. A thermochemical database for the solar cell silicon materials. *Materials Transactions*, 50(8):1978–1984, Jul 2009.

[58] S Myers, M Seibt, and W Schröter. Mechanisms of transition-metal gettering in silicon. *Journal of Applied Physics*, Jan 2000.

[59] M Morita, T Ohmi, E Hasegawa, M Kawakami, and K Suma. Control factor of native oxide growth on silicon in air or in ultrapure water. *Applied Physics Letters*, 55:562, 1989.

[60] A. A Istratov, P Zhang, R. J Mcdonald, A. R Smith, M Seacrist, J Moreland, J Shen, R Wahlich, and E. R Weber. Nickel solubility in intrinsic and doped silicon. *Journal of Applied Physics*, 97(2):023505, Jan 2005.

[61] AA Istratov, W Huber, and ER Weber. Experimental evidence for the presence of segregation and relaxation gettering of iron in polycrystalline silicon layers on silicon. *Applied Physics Letters*, 85:4472, 2004.

[62] AA Istratov, H Hedemann, M Seibt, OF Vyvenko, W Schroter, T Heiser, C Flink, H Hieslmair, and ER Weber. Electrical and recombination properties of copper-silicide precipitates in silicon. *Journal of The Electrochemical Society*, 145(11):3889–3898, Jan 1998.

[63] S Hudelson. High temperature investigations of crystalline silicon solar cell materials. Master's thesis, MIT, 2009.

[64] Ultra high temperature systems - ts1500, ts1200 and ts1000. Technical report, Linkam Scientific Instruments.

[65] B. L. Henke, E. M. Gullikson, and J. C. Davis. X-ray interactions: Photoabsorption, scattering, transmission, and reflection at e = 50-30,000 ev, z = 1-92. *Atomic Data and Nuclear Data Tables*, 54(2):181–342, July 1993.

[66] T Sato. Spectral emissivity of silicon. *Japanese Journal op Applied Physics Vol*, 6(3), 1967.

[67] MA Marcus, AA MacDowell, R Celestre, A Manceau, T Miller, HA Padmore, and RE Sublett. Beamline 10.3.2 at als: a hard x-ray microprobe for environmental and materials sciences. *J Synchrotron Radiat*, 11:239–247, Jan 2004.

[68] Matthew A Marcus. http://xraysweb.lbl.gov/uxas/index.htm.

[69] B Ravel and M Newville. Athena, artemis, hephaestus: data analysis for x-ray absorption spectroscopy using ifeffit. *Journal of Synchrotron Radiation*, 12:537–541, Jan 2005.

[70] M Seibt, H Hedemann, A Istratov, and F Riedel. Structural and electrical properties of metal silicide precipitates in silicon. *physica status solidi (a)*, Jan 1999.

[71] A Filipponi, M Borowski, P Loeffen, and S De .... Single-energy x-ray absorption detection: a combined electronic and structural local probe .... *Journal of Physics: Condensed Matter*, Jan 1998.

[72] J H Aalberts and M L Verheijke. The solid solubility of nickel in silicon determined by neutron activation analysis. *Applied Physics Letters*, 1(1):19–20, Jan 1962.

[73] N Wiehl, U Herpers, and E Weber. Study on the solid solubility of transition metals in high-purity silicon by instrumental .... *Journal of Radioanalytical and Nuclear Chemistry*, Jan 1982.

[74] Masayuki Yoshida and Katsuhisa Furusho. Behavior of nickel as an impurity in silicon. *Japanese Journal of Applied Physics*, 3(9):521–529, Nov 1964.

[75] FA Trumbore. Solid solubilities of impurity elements in germanium and silicon. *Bell System Technical Journal*, 39:205–233, Feb 1960.

[76] B. Rygalin, V. Prokofieva, L. Pavlova, and Y.E. Sokolov. The si-sr and si-ba phase diagrams over the si-rich composition range. *Calphad*, 34(2):196 – 199, 2010.

[77] T Yoshikawa and K Morita. Removal of b from si by solidification refining with si-al melts. *Metall Mater Trans B*, 36(6):731–736, Jan 2005.

[78] T Yoshikawa, K Arimura, and K Morita. Boron removal by titanium addition in solidification refining of silicon with si-al melt. *Metall Mater Trans B*, 36(6):837–842, Jan 2005.

[79] Takeshi Yoshikawa and Kazuki Morita. Removal of phosphorus by the solidification refining with si-al melts. *Science and Technology of Advanced Materials*, 4:531–537, Mar 2003.

[80] S Langkau, M Heuer, HJ Höbler, K Bente, and G Kloess. Miscibility of nisi2, fesi2 and cu3si. *Journal of alloys and compounds*, 474(1-2):334–340, 2009.